

Theoretical Study of Electronic Transport in Two-Dimensional Transition Metal Dichalcogenides: Effects of the Dielectric Environment

Sanjay Gopalan, Maarten L. Van de Put,^{*} Gautam Gaddemane,^{*} and Massimo V. Fischetti[†]

*Department of Materials Science and Engineering,
The University of Texas at Dallas*

800 W. Campbell Rd., Richardson, TX 75080

(Dated: August 24, 2022)

We discuss the effect of the dielectric environment (substrate/bottom oxide, gate insulator, and metal gates) on electronic transport in two-dimensional (2D) transition metal dichalcogenides (TMD) monolayers. We employ well-known *ab initio* methods to calculate the low-field carrier mobility in free-standing layers and use the dielectric continuum approximation to extend our study to layers in double-gate structures, including the effects of dielectric screening of the electron-phonon interaction caused by the bottom oxide and the gate insulator, and of scattering with hybrid interface optical-phonon/plasmon excitations (‘remote phonon scattering’). We find that the presence of insulators with a high dielectric constant may improve significantly the carrier mobility. However, scattering with the interface hybrid excitations negates this gain and degrades the mobility significantly below its free-standing value. We find that this process is dominated by long-wavelength interactions that, for the carrier sheet-density of interest, are strongly affected by the coupling with the 2D plasmons. Considering 2D layers in a double-gate geometry with SiO₂ as bottom-oxide and various top-gate insulators, we find that the mobility decreases as the top-insulator dielectric constant increases (from hBN to ZrO₂), as expected. However, we observe two main deviations from this trend: A high mobility is predicted in the case of the weakly polar hBN, and a mobility much lower than expected is calculated in the case of gate-insulator/TMD/bottom-oxide stacks in which two or more polar materials have optical-phonon with similar resonating frequencies. We also find that the effect of screening by metal gates is noticeable but not particularly strong. Finally, we discuss the effect of the TMD dielectric constant, of the free-carrier density, and of temperature on the transport properties of TMD monolayers.

I. INTRODUCTION

A. Supported and gated 2D materials

The recent interest in two-dimensional (2D) materials, motivated by the search for alternatives to Si in the very large scale integration (VLSI) technology, has benefited from recent advances in density functional theory (DFT) that now permits the calculation not only of the excitation spectrum of a crystal, but also of the electron-phonon matrix elements and of the low-field carrier mobility (see, for example, Refs. [1] and [2]). Indeed, limiting our attention to transition metal dichalcogenides (TMD) monolayers, that constitute the focus of our work, *ab initio* methods have been used to predict the carrier mobility in a variety of them, for example by Jin and coworkers [3], by Gunst *et al.* [4], by Sohler and coworkers [1], and by Rawat *et al.* [5]. For MoS₂ in particular, similar studies have been reported by Kaasjberg and coworkers [6], by Restrepo *et al.* [7], by Li and coworkers [8], and by our own group [9]. An *ab initio* study of quantum electron transport in MoS₂ field effect transistors (FETs) has also been reported by Szabó *et al.* [10].

Unfortunately, so far the vast majority of these first-principles studies have focused mainly on electronic

transport in *ideal free-standing* layers (with the notable exceptions discussed in the next subsection), ignoring the effect that the dielectric environment (that is, the insulating substrate, the gate insulator(s), and the metal gates) may have on the charge-transport characteristics of the material. These are more than mere deviations from ideality, since in almost all applications the monolayers are supported by an insulating substrate and must be gated, implying the presence of a gate insulator and gate contact(s). Therefore, charge transport in these van der Waals (vdW) monolayers is controlled not only by their ‘bulk’ properties, but also by the proximity of these polar insulators. Their influence goes beyond process-dependent effects, such as the presence of defects, charge impurities, non-ideal interfaces, which one may always hope to minimize by optimizing the technology, much as in the case of interface roughness for Si-based devices. Indeed, the dielectric polarization of the top and bottom insulators may screen the ‘out-of-plane’ electric-field lines, enhancing screening of all Coulomb interactions, including scattering with the 2D phonons of the monolayers. Moreover, the plasma excitations of the two-dimensional electron gas (2DEG, the monolayer) and the optical phonons present in the system (substrate, gate insulator, and the 2D layer itself, if polar) contribute to the formation of hybrid interface excitations resulting from the coupling of these eigenmodes of the system. Scattering of electrons (and holes) with these hybrid interface plasmon/optical-phonon excitations (IPPs) is an additional process that affects electronic transport. This

^{*} Present address: imec, Kapeldreef 75, B-3001 Leuven, Belgium

[†] email: max.fischetti@utdallas.edu.

process goes under the somewhat improper name of ‘remote phonon scattering’. Here we shall avoid the use of this confusing term and refer to it more appropriately as to ‘IPP scattering’.

Before moving to the main subject of this work, we should point out that charge carriers may interact with excitations at the interface between the TMD layer and the insulator not only via the polar (Fröhlich-like) interactions that we consider here, but also via nonpolar (deformation-potential) interactions. An *ab initio* study of these nonpolar processes at the MoS₂/hBN interface has been presented recently by Fiore *et. al* [11]. Their effect on charge transport appears to be small, so we shall ignore them here. However, they may affect the thermal properties of material.

B. Overview of previous work on electron-IPP scattering

Scattering with these hybrid IPPs, or simply scattering with interface optical modes decoupled from 2D plasmons (SOs), has been investigated at length in the past employing the dielectric continuum approximation (that we shall adopt here). Scattering of electrons with surface optical modes at the Si/SiO₂ interface was first considered by Wang and Mahan [12], already in 1972, starting from Fuchs and Kliever’s work [13]. Taking hint from this study, the issue was reconsidered by Hess and Vogl [14] (who coined the term ‘remote phonons’) – ironically suggesting the use of low- κ gate insulators to boost the electron mobility in Si inversion layers –, by Moore and Ferry [15], and by Bechstedt and Enderlein [16] – accounting for the dependence of the process on the 2D carrier density – in the 1980s. Full coupling to polycrystalline-Si gate and inversion-layer 2D plasmons (important at the long wavelengths at which the interaction is strong) was considered by Fischetti *et al.* [17] in 2001, although Toniutti *et al.* [18], in critically revisiting the problem a decade later, argued that plasmon-phonon hybridization does not play any major role (at least in the Si/SiO₂ system and at sufficiently short wavelengths. We shall show below that this is not the case, at least in the systems considered here).

The study of electron scattering with the IPPs and/or SOs also been extended to other materials and interfaces: To supported and/or gated graphene [19–23], to carbon nanotubes [24], to Si nanowires [25], to III-V [26–29], and to III-nitrides heterostructures [30, 31].

Coming to the structures considered here, several studies have been performed in the past using a variety of approximations: Zeng *et al.* [32] considered supported and gated MoS₂ monolayers, ignoring coupling to plasmons. The dependence of the SO scattering strength on the dielectric environment in MoS₂ monolayers sandwiched between a substrate and a gate insulator was also studied by Ma and Jena [33], also ignoring the full coupling to plasmons and using a simplified form of the scattering potential. The same simplified model was employed by

Hosseini *et al.* [34] to study strained TMDs. Supported and gated InSe monolayers were considered by Chang and co-workers [35], also ignoring coupling to plasmons, but considering the screening effect of a metal gate.

Of particular interest is the work done by Hauber and Fahy [36]. They have performed an analysis of the plasmon/optical-phonon excitations in several bulk III-V compound semiconductors and in supported-and-gated hBN and MoS₂ monolayers. Their analysis bypasses many of the approximations employed in all the previous studies that we have just mentioned. In particular, they have considered fully the plasmon-phonon coupling, also accounting (correctly) for the IPP lifetime (and, so, for Landau damping), treating electron and IPP transport self-consistently. However, given the complexity of their formulation, they have analyzed only one TMD system (supported and gated MoS₂ but without gate screening) and a limited set of dielectrics (SiO₂ and HfO₂), in addition to vacuum. Moreover, they did not use *ab initio* methods to deal with band-structure-related effects entering the calculation of other scattering processes (mainly, scattering with bulk TMD phonons).

Finally, of note is a comprehensive study of IPPs in vdW heterostructures performed by Zhang and co-workers [37], showing experimentally the existence of these modes and the validity of the long-wavelength approximation used to compute their dispersion. This is notable because the term ‘remote phonons’ has caused some confusion: As recently shown by Dyson and Ridley [38], what may be properly called electron scattering with ‘remote-phonons’ (that is: electrons in the semiconducting layer interacting with the dipole field generated by optical phonons in an adjacent insulator) is a process with negligible strength. Unfortunately, as we have already remarked, this term has come to label improperly the very different process we consider here, namely, electron scattering with the hybrid interface excitations.

Experimental information that may confirm conclusively the importance of electron-IPP scattering is still controversial. While the degradation of the mobility in channels supported and/or gated by high- κ dielectrics is well established, alternative processes, such as remote Coulomb scattering [39–42] or scattering with interface dipoles [43], have been proposed to explain the observations. As a result, whereas several studies claim to have proven experimentally that the carrier mobility is controlled by electron-IPP scattering, (for example, Ref. [44] for the Si/SiO₂ system, Ref. [45] for the InGa_{0.53}As_{0.47}/HfO₂ stacks, or Ref. [46] for MoS₂ supported by SiO₂, HfO₂, or Al₂O₃), other experimental studies have found that the observed mobility degradation is due mainly some of these alternative processes, such interface dipoles [43] or Coulomb scattering [47].

Even more controversial is the possibility that an ideal metal gate may screen the IPP scattering potential: No evidence of this effect has been reported by Maitra *et al.* in Si metal-oxide-semiconductor FETs (MOSFETs) [48]; however, it has been observed in other systems, such

as organic and InGaZnO thin-film transistors [49, 50]. Laikhtman and Solomon have even predicted theoretically anti-screening effects due to a metal gate [51].

Another gate-related effect is the predicted depression of the electron mobility in polycrystalline Si (poly-Si) gate MOSFETs due to a resonance between gate plasmons and insulator optical-phonons. This has been proposed by Kotlyar *et al.* [52], by Shah and De Souza [53], and by Suleiman *et al.* [54]. This, as well as the other issue mentioned above, will be discussed below.

C. Aim and organization of this work

The aim of this work is to provide a comprehensive study of the effect of IPP scattering on the low-field mobility of electrons and holes, mostly at 300 K, employing physical models – within the dielectric continuum approximation – that bypass several approximations that are often used. Namely, we employ *ab initio* (DFT) methods to calculate the band structure of the TMDs, the 2D ‘bulk’ phonon dispersion, and the electron-phonon matrix elements; we account fully for the presence of the dielectrics by considering not only scattering with fully hybridized IPPs but also for the screening effects of the insulators on the strength of the interaction with bulk 2D phonons (an effect not considered previously) and, finally, we consider also the role played by nearby ideal-metal gates in screening both the bulk electron-phonon and IPP scattering. Finally, we use full-band Monte Carlo simulations to calculate the low-field mobility, thus addressing concerns raised by Toniutti *et al.* [18]. In this study we consider a variety of hexagonal TMD monolayers (MoS₂, MoSe₂, MoTe₂, WS₂, WSe₂, and also WTe₂[55]) in a double-gate structure ‘sandwiched’ between a SiO₂ bottom-gate-insulator and several gate insulators (SiO₂, hBN, AlN, Al₂O₃, HfO₂, and ZrO₂).

The main results of our work can be summarized as follows: The presence of a bottom insulator and/or a gate insulator with a high dielectric constant (high- κ insulators) screens the interaction of electrons (and holes) with the bulk (2D) phonons of the monolayer. Whereas, in principle, this has a strong beneficial effect on the carrier mobility, IPP scattering depresses the mobility below its free-standing value, with the notable exception of hBN, as already found by Ma and Jena [33], since it is only weakly polar and the frequencies of its optical phonons are large enough to be decoupled from all other frequencies entering the problem. Moreover, the carrier mobility follows the expected trend, decreasing with increasing dielectric constant of the gate insulator; however, there are significant deviations from this behavior: In gate-insulator/TMD/SiO₂ structures in which two or more optical-phonon frequencies are similar, resonance of these modes causes an enhanced interface polarization charge, resulting in a very low mobility. Finally, the screening effect of the ideal-metal gate is noticeable, but not particularly strong.

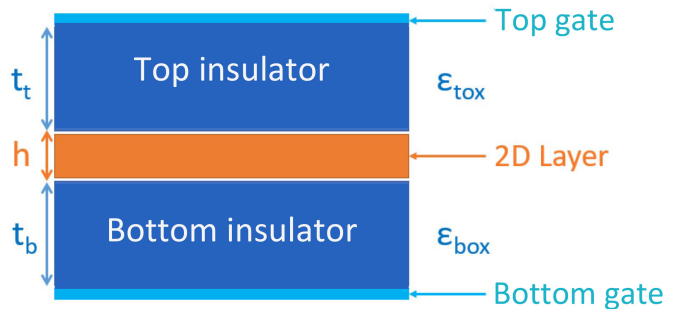


FIG. 1. Schematic diagram of the double-gated TMD monolayer considered here.

We organize our discussion as follows: In Section II, we present the theoretical model and computational methods used to calculate the carrier mobility in different monolayer TMDs accounting for presence of different dielectric environments. In Section III, we present results for the carrier mobility in the various TMD monolayers we have considered and discuss in-detail how the dielectric environment affect their transport properties. Finally, we present our conclusions in Sec. IV.

II. THEORETICAL MODEL

Throughout our discussion, we use the dielectric-continuum limit, the long-wavelength limit of the dielectric ionic response of all materials; and, for the insulators, we ignore details about their morphology (crystalline, polycrystalline, or amorphous), treating them as isotropic amorphous media. Furthermore, we consider only a maximum of two optical phonons per material, those with the largest oscillator strength, as measured by Fourier-transform infrared spectroscopy, as explained in Ref. [17].

As a matter of notation, we employ lower-case bold symbols (such as \mathbf{r} or \mathbf{k}) to denote 3-vectors and upper-case bold symbols (such as \mathbf{R} or \mathbf{K}) to denote 2-vectors on the (x, y) plane of the layer. We use SI units and denote by e the magnitude of the electron charge, by m_0 the free electron mass, by ϵ_0 the permittivity of vacuum, by \hbar the reduced Planck’s constant, by T the absolute temperature, and by k_B Boltzmann’s constant. Other quantities will be defined as needed. Finally, to avoid a cumbersome notation with too many subscripts, occasionally we shall be guilty of using an improper notation by denoting the functional dependence of several quantities on independent variables as subscripts or within parentheses (*e.g.*, $\epsilon(Q, \omega)$ or $\epsilon_{Q, \omega}$), regardless of whether we use finite-volume or infinite-volume normalization.

A. The system

The system we consider, shown in Fig. 1, consists of an ideal (bottom) metal gate in the region $z \leq -t_b$; an in-

sulator (which can be viewed either as a substrate, when $t_b \rightarrow \infty$), or as a bottom gate insulator) with dielectric function $\epsilon_{\text{box}}(\omega)$ in the region $-t_b < z \leq 0$; a 2D layer of thickness h and dielectric function $\epsilon_{2D}(Q, \omega)$ in the region $0 < z \leq h$; a gate insulator with dielectric function $\epsilon_{\text{tox}}(\omega)$ in the region $h < z \leq h + t_t$; an ideal metal in the half-space $z > h + t_t$. Ignoring the confinement of the lattice vibrations in thin layers, an effect that may weaken the ionic dielectric response of thin dielectrics and has been studied by Laikhtman and Solomon [51], for the insulators we assume the 'bulk' long-wavelength limit of the dielectric functions, dependent on the frequency ω , assuming only two optical phonons in each oxide, as explained above:

$$\begin{aligned} \epsilon_{\text{box}}(\omega) &= \epsilon_{\text{box}}^{(\infty)} + [\epsilon_{\text{box}}^{(0)} - \epsilon_{\text{box}}^{(\text{mid})}] \frac{\omega_{\text{TO},1}^2}{\omega_{\text{TO},1}^2 - \omega^2} + \\ &[\epsilon_{\text{box}}^{(\text{mid})} - \epsilon_{\text{box}}^{(\infty)}] \frac{\omega_{\text{TO},2}^2}{\omega_{\text{TO},2}^2 - \omega^2} = \epsilon_{\text{box}}^{(\infty)} \frac{\omega_{\text{LO},1}^2 - \omega^2}{\omega_{\text{TO},1}^2 - \omega^2} \frac{\omega_{\text{LO},2}^2 - \omega^2}{\omega_{\text{TO},2}^2 - \omega^2}, \quad (1) \\ \epsilon_{\text{tox}}(\omega) &= \epsilon_{\text{tox}}^{(\infty)} + [\epsilon_{\text{tox}}^{(0)} - \epsilon_{\text{tox}}^{(\text{mid})}] \frac{\omega_{\text{TO},3}^2}{\omega_{\text{TO},3}^2 - \omega^2} + \\ &[\epsilon_{\text{tox}}^{(\text{mid})} - \epsilon_{\text{tox}}^{(\infty)}] \frac{\omega_{\text{TO},4}^2}{\omega_{\text{TO},4}^2 - \omega^2} = \epsilon_{\text{tox}}^{(\infty)} \frac{\omega_{\text{LO},3}^2 - \omega^2}{\omega_{\text{TO},3}^2 - \omega^2} \frac{\omega_{\text{LO},4}^2 - \omega^2}{\omega_{\text{TO},4}^2 - \omega^2}, \quad (2) \end{aligned}$$

having indicated with $\omega_{\text{TO},1}$ and $\omega_{\text{TO},2}$ the low- and high-frequency optical phonons of the substrate insulator, with $\omega_{\text{TO},3}$ and $\omega_{\text{TO},4}$ the low- and high-frequency optical phonons of the gate insulator, and with $\epsilon^{(0)}$, $\epsilon^{(\text{mid})}$ and $\epsilon^{(\infty)}$ the static, intermediate, and optical dielectric constants of the insulators. As mentioned above, since we assume amorphous insulators, it is reasonable to treat them as isotropic dielectrics, we do not need to specify whether these dielectric functions are transverse or longitudinal components of the full dielectric tensor. This is not the case for the 2D TMD monolayer. In this case, we assume for the out-of-plane dielectric function for the 2D layer:

$$\begin{aligned} \epsilon_{2D\perp}(Q, \omega) &= \epsilon_{2D\perp}^{(\infty)} [1 - e^2 G_Q(h/2, h/2) \Pi_{2D}(Q, \omega)] + \\ &[\epsilon_{2D\perp}^{(0)} - \epsilon_{2D\perp}^{(\infty)}] \frac{\omega_{\text{ZO}}^2}{\omega_{\text{ZO}}^2 - \omega^2}, \quad (3) \end{aligned}$$

where Q is the magnitude of the wave vector on the plane of the layer, $\epsilon_{2D\perp}^{(\infty)}$ and $\epsilon_{2D\perp}^{(0)}$ are the the out-of-plane optical and static dielectric constants (as calculated via DFT together with the dielectric thickness h , as given in Ref. [56], or via the formalism of Ref. [57]). The function $G_Q(z, z')$ is the in-plane Fourier transform of the Poisson Green's function for the geometry of interest; it represents the potential at $z = h/2$ (in the middle of the monolayer) caused by a point-charge also at $z' = h/2$. This will be discussed below (see Eqs. (19)-(22)) for the general double-gate geometry. The quantity $\Pi_{2D}(Q, \omega)$

is the polarizability of the free carriers in the 2D layer as given, for example, by Stern [58] or by the simpler approximation given below. Finally, the last term in Eq. (3) reflects the out-of-plane ionic polarization of the monolayer; obviously, it is present only in the case of a polar 2D layer with out-of-plane optical phonons, ZO, with frequency ω_{ZO} [59].

Regarding the anisotropy of the dielectric constant of the TMD layer, an approximation that bypasses several subtle issues, and that we employ here, consists in defining an 'effective' dielectric constant $\epsilon_{2D}^{(\text{eff})} = \epsilon_{2D\perp}(\epsilon_{2D\parallel}/\epsilon_{2D\perp})^{1/2}$, as suggested by Hauber and Fahy [36]. Regardless of the assumption made, in the following we shall omit the subscripts ' \perp ' or superscript 'eff', since only the out-of-plane or effective dielectric function of the 2D layer will be used.

We must stress that in the σ_h -symmetric layers we consider here (*i.e.*, the 2H TMD monolayers that are symmetric under reflections on the (x, y) plane), the polarization caused by the ZO-phonon polarization induces a potential that is antisymmetric with respect to the layer of the transition-metal ions, Mo or W [59]. Therefore, at first-order, the matrix elements of the scattering potential associated with such an antisymmetric potential vanishes. In other words, electrons do not couple to the out-of-plane (ZO) component of the hybrid modes that we shall consider below.

At a finite temperature, the expression for the zero-temperature electronic polarizability $\Pi_{2D}(Q, \omega)$ given by Stern [58], could be replaced by the well-known finite-temperature expression given by Maldague [60]. Unfortunately, its use results in numerical complications, since solving the secular equations that we shall consider below – required to obtain the dispersion of the hybrid interface modes of interest here – would not consist on finding the roots of a polynomial, but on the much more difficult task of finding the roots of a transcendental equation.

This difficulty can be circumvented by noticing that the expressions given by Eqs. (1) and (2) are valid only in the long-wavelength limit $Q \rightarrow 0$. Therefore, in the same long-wavelength spirit, the electronic contribution to Eq. (3) (that is, of the free-carriers term given by the first term at the right-hand side of Eq. (3)) can be approximated by the simpler expression:

$$\epsilon_{2D}^{(\text{el})}(Q, \omega) \approx \epsilon_{2D}^{(\infty)} \left[1 - \frac{\omega_P(Q)^2}{\omega^2} \right], \quad (4)$$

having defined the 2D plasma dispersion $\omega_P(Q)^2 = e^2 n Q / (2\epsilon_{2D}^{(\infty)} m^*)$, where n is the density of the free carriers and m^* their effective mass. This expression captures the small- Q behavior in the region in which the response is not strongly damped by a large imaginary part; that is, outside the single-particle region in which $E(\mathbf{k}_F + \mathbf{Q}) - E(\mathbf{k}_F) = \hbar\omega$ (\mathbf{k}_F being the Fermi wave vector). Moreover, in this range of long wavelengths, there is no significant dependence on temperature between 0 and 300 K. Therefore, to simplify the numerical complexity of the formulation and without making any severe error,

TABLE I. Parameters used for the density functional theory (DFT) and density functional perturbation theory (DFPT) calculations.

Parameters	
Kinetic energy (E_k) cutoff	60 Ry
Charge density cutoff	240 Ry
Ionic minimization threshold	10^{-6} Ry
Self-consistent field threshold	10^{-12} Ry
\mathbf{k} -point mesh	$12 \times 12 \times 1$

we can use Eq. (4) as long as wavelength of the perturbation is longer than the ‘Landau damping’ wavelength, $\sim 1/Q_{\text{LD}}$, defined implicitly by:

$$Q_{\text{LD}} = \left[k_{\text{F}}^2 + \frac{2m^* \omega_{\text{P}}(Q_{\text{LD}})}{\hbar} \right]^{1/2} - k_{\text{F}}. \quad (5)$$

The use of this expression in the long-wavelength limit, $Q \rightarrow 0$, is also consistent with the range of validity of Eqs. (1) and (2). On the contrary, for $Q > Q_{\text{LD}}$, we may treat the response of the free carriers in the 2D layer as purely static using the Q -dependent Thomas-Fermi expression, as discussed below before Eq. (32). The problem of how to account correctly for Landau damping – and how we have tackled the problem – will be discussed below in Sec. IID 2.

We have calculated the plasma frequency, $\omega_{\text{P}}(Q)$ that appears in Eq. (4) ignoring the possibility that electrons populating the satellite Q valleys (sixfold degenerate minima located along the K– Γ -direction) may result in a different plasma response. The coupled plasma oscillations of two two-dimensional electron gases, characterized by a different effective mass and density, have been studied by Vignale [61]. He found that this situation results in the presence of two plasma modes: A ‘fast’ optical plasmon corresponding, in our case, to electrons in the K and Q valleys oscillating in phase, and a ‘slow’ acoustic mode associated with K and Q electrons oscillating out of phase. However, in all the materials and in the near-equilibrium situations considered here, the energy of the satellite Q-valleys is sufficiently larger than $k_{\text{B}}T$ as to render the electron density in this valleys only a small fraction of the total density. For example, the six satellite Q-valleys in MoS₂ are at an energy between 70 and 270 meV (the value we obtain using the pseudopotentials and exchange-correlation functionals chosen here [9]) above the minima at the symmetry points K. Therefore, we have simplified the problem by employing Eq. (4) to account for the response of the optical plasmon, while ignoring the effect of the few electrons in the satellite valleys. Moreover, we have ignored the acoustic plasmon since, as shown by Vignale [61], for a small occupation of the satellite valleys, it will be strongly Landau-damped by the fast optical plasmon.

B. *Ab initio* calculations

In order to obtain the electronic band structures, phonon dispersion, and electron-phonon matrix elements in the 2H-TMDs of interest, we have employed *ab initio* methods that have become almost ‘routine’. Here, we shall give here only the essential information. We should note that, in obtaining the results presented in this section, we have ignored possible corrections caused by a non-zero temperature and the presence of a gate bias.

We have used density functional theory (DFT) as implemented in the Quantum ESPRESSO (QE) package [62] with the Perdew–Burke–Ernzerhof generalized-gradient approximation (GGA-PBE) [63] for the exchange-correlation functional, and the norm-conserving Vanderbilt pseudopotentials (ONCV) [64] for each constituent element. The atomic structure for these materials is found by minimizing the total energy with respect to the lattice constants and ionic positions. The computational parameters used in these calculations are shown in Table I. As required by the Monte Carlo simulations described in Ref. [9, 65, 66] and used here, the band structure is tabulated on a fine mesh, $201 \times 201 \times 1$, covering a rectangular section that inscribes the triangular irreducible wedge of the hexagonal first Brillouin zone. For the calculation of the phonon dispersion and of the electron–phonon matrix elements, we have used the ‘Electron–Phonon Wannier’ (EPW) software package [67–70] which uses density functional perturbation theory (DFPT). These quantities are initially calculated on a coarse \mathbf{k} - ($12 \times 12 \times 1$) and \mathbf{q} -mesh ($6 \times 6 \times 1$) and interpolated on finer \mathbf{k} - ($30 \times 30 \times 1$) and \mathbf{q} -meshes ($30 \times 30 \times 1$) using maximally-localized Wannier functions. The coarse and the fine meshes span the entire Brillouin zone. The phonon dispersion and electron–phonon matrix elements on the fine mesh are finally interpolated on the band structure mesh using a bilinear interpolation. The phonon-limited electron–phonon scattering rates are calculated using Fermi’s golden rule, and tabulated on the same mesh of \mathbf{k} -points used to tabulate the band structure.

We have not considered the effect of spin-orbit coupling (SOC) since, as shown in our previous work [9], it affects the calculated electron mobility only marginally, by less than 10%, in the cases of MoS₂ and MoTe₂, although its effect is larger for WS₂ and it may affect the hole mobility more significantly. As we shall see below, the effects of dielectric screening of the surrounding insulators and of IPP scattering are much larger than those caused by SOC. Therefore, we expect that ignoring the numerically cumbersome effects of SOC is not going to alter significantly the qualitative trends of our results and, in the cases of MoS₂ and MoTe₂, not even quantitatively.

C. Screening of the electron-phonon interaction by the dielectric environment

The electron-phonon matrix elements calculated using DFT assume free-standing layers, since the calculations are performed using a supercell consisting of the isolated layer surrounded by sufficiently 'thick' vacuum padding to isolate adjacent supercells. Of course, it would be desirable to perform the calculations using a more complicated and larger supercell that includes the dielectrics and the gates, also accounting for the presence of free carriers in the monolayer. In so doing, one would obtain information about confined phonons in the insulators and interface polarization charges, for example. However, this task is extremely complex. Therefore, in order to consider how the electron-phonon interaction is affected by the presence of the dielectrics and of the metal gates, we consider how the electron-phonon matrix elements calculated using DFT depend on the Poisson Green's function and replace it with the Green's function that satisfies the boundary conditions of the double-gate structures of interest here. Although we are forced to make use of some simplifications and approximations, the procedure should capture the main physics of the process.

First, we note that the matrix elements between two Bloch states \mathbf{k} in band n and \mathbf{k}' in band n' obtained from DFT have the form:

$$\langle \mathbf{k}', n' | \delta \mathbf{E}_{\text{tot}}^{(\eta)} | \mathbf{k}, n \rangle = \int d\mathbf{r} \psi_{\mathbf{n}', \mathbf{k}'}^*(\mathbf{r}) \delta \mathbf{E}_{\text{tot}}^{(\eta)}(\mathbf{r}) \psi_{\mathbf{n}, \mathbf{k}}(\mathbf{r}), \quad (6)$$

where $\psi_{\mathbf{n}, \mathbf{k}}(\mathbf{r}) = e^{i\mathbf{k}\cdot\mathbf{r}} \sum_{\mathbf{g}} u_{\mathbf{k}, \mathbf{g}}^{(n)} e^{i\mathbf{g}\cdot\mathbf{r}} / \Omega^{1/2}$ is the Bloch wave of the TMD layer ($\Omega = N_{\text{cell}} \Omega_{\text{cell}}$ is the normalization volume and the 3-vectors \mathbf{g} are the vectors in reciprocal space) and $\delta E_{\text{tot}}^{(\eta)}(\mathbf{r})$ is the change of the total energy of the system caused by a phonon of branch (acoustic/optical, longitudinal/transverse/flexural) η . Perhaps too pedantically, we have expressed the electronic states as dependent on the 3-vector $\mathbf{k} = (\mathbf{K}, k_z)$, since they are obtained from DFT calculations that employ a three-dimensional supercell. However, since we are interested only in states with energy much below the vacuum level, we could ignore their dependence on the out-of-plane component, k_z , and write, instead, $\psi_{\mathbf{K}}(\mathbf{r})$, a notation that we shall use in the following.

Both the Hartree and the exchange-correlation potentials contribute to this change; that is (oversimplifying the notation in writing exchange and correlation as a local potential), $\delta E_{\text{tot}}^{(\eta)}(\mathbf{r}) = \delta E_{\text{H}}^{(\eta)}(\mathbf{r}) + \delta E_{\text{xc}}^{(\eta)}(\mathbf{r})$. These are the quantities that need to be modified when considering the more complicated geometry of interest. Now we note that the Hartree energy, $E_{\text{H}}(\mathbf{r})$, depends linearly on the electron density, whereas $E_{\text{xc}}(\mathbf{r})$ has a weaker dependence (namely, $E_{\text{xc}}(\mathbf{r}) \sim \rho^{(n)}(\mathbf{r})^{1/3}$ in the local-density approximation). Therefore, we expect that the exchange-correlation terms will have a contribution to the scattering rates smaller than the Hartree term under a modification of the dielectric environment. Thus, we consider

only the Hartree component whose contribution, in the case of a free-standing layer, as done using DFT, can be written as:

$$\delta E_{\text{tot}}(\mathbf{r}) \approx \delta E_{\text{H}}^{(\eta)}(\mathbf{r}) = \int d\mathbf{r}' G^{(0)}(\mathbf{r}, \mathbf{r}') \delta \rho^{(\eta)}(\mathbf{r}'), \quad (7)$$

where $G^{(0)}(\mathbf{r}, \mathbf{r}')$ is the Green's function for the Poisson equation *in vacuo* and $\delta \rho^{(\eta)}(\mathbf{r}')$ is the change of the charge at \mathbf{r}' induced by a phonon of branch η . This can be written as:

$$\delta \rho^{(\eta)}(\mathbf{r}') = \sum_{\alpha l} \tilde{\nabla}_{\mathbf{R}_{\alpha l}} \rho(\mathbf{r}') \cdot \delta \mathbf{r}_{\alpha l}^{(\eta)}, \quad (8)$$

where the quantity $\delta \mathbf{r}_{\alpha l}^{(\eta)}$ is the displacement of the ion α in cell l due to phonons of branch η . The symbol $\tilde{\nabla}$ should be interpreted as a 'functional gradient', so that the function $\tilde{\nabla}_{\mathbf{r}_{\alpha l}} \rho(\mathbf{r})$ (often written as $\delta \rho(\mathbf{r}) / \delta \mathbf{r}_{\alpha l}$) represents the change of the electronic charge ρ at position \mathbf{r} under an infinitesimal shift of ion α in cell l along the Cartesian directions. This can be obtained from the 'small displacement method' (implemented, for example, in the computer program PHON [71]) or from DFPT [68]. We now write $\mathbf{r}_{\alpha l} = \mathbf{r}_l + \boldsymbol{\tau}_{\alpha}$, where \mathbf{r}_l is the lattice site l and $\boldsymbol{\tau}_{\alpha}$ is the position of ion α in the unit cell.

We now consider only in-plane phonons (since, as explained above, scattering with out-of-plane vibrations is forbidden at first order in the symmetric TMDs we consider), also consider negligible their displacement and any change of the charge density they induce along the z direction. Therefore, using the usual expression for $\delta \mathbf{r}_{\alpha l}^{(\eta)}$ and tracing over the phonon states assumed to be at thermal equilibrium, the charge density obtained from DFT, Eq. (8), can be expressed approximately as:

$$\begin{aligned} \delta \rho^{(\eta)}(\mathbf{r}') \approx & \sum_{\alpha l \mathbf{Q}} \tilde{\nabla}_{\mathbf{r}_{\alpha l}} \rho(\mathbf{r}') e^{i\mathbf{Q}\cdot\mathbf{r}_{\alpha l}} \cdot \mathbf{e}_{\parallel \mathbf{Q}}^{(\eta, \alpha)} \\ & \times \left(\frac{\hbar}{2M_{\alpha} \omega_{\mathbf{Q}}^{(\eta)}} \right)^{1/2} \left\{ \begin{array}{l} N(\omega_{\mathbf{Q}}^{(\eta)})^{1/2} \\ [1 + N(\omega_{\mathbf{Q}}^{(\eta)})]^{1/2} \end{array} \right\} = \\ & \sum_{\alpha l \mathbf{Q}} A_{\mathbf{Q}}^{(\eta, \alpha)} e^{i\mathbf{Q}\cdot\mathbf{r}_{\alpha l}} \mathbf{e}_{\parallel \mathbf{Q}}^{(\eta, \alpha)} \cdot \tilde{\nabla}_{\mathbf{r}_{\alpha l}} \rho(\mathbf{r}'), \quad (9) \end{aligned}$$

where the quantity $A_{\mathbf{Q}}^{(\eta, \alpha)}$ is defined implicitly by the last equality, $\mathbf{e}_{\parallel \mathbf{Q}}^{(\eta, \alpha)}$ and $\omega_{\mathbf{Q}}^{(\eta)}$ are the in-plane polarization (for the ion α) and frequency of a phonon of branch η and wave vector \mathbf{Q} , $N(\omega_{\mathbf{Q}}^{(\eta)})$ is the Bose-Einstein occupation of such phonons, and M_{α} is the mass of the ion α . The upper and lower quantities in the curly bracket refer to absorption and emission processes, respectively. Also, note that $\mathbf{r}_{\alpha l}$ is a 3-vector but \mathbf{Q} is a 2-vector; thus, the inner product $\mathbf{Q}\cdot\mathbf{r}_{\alpha l}$ should be understood as $\mathbf{q}\cdot\mathbf{r}_{\alpha l}$, where $\mathbf{q} = (\mathbf{Q}, 0)$. Similarly, $\mathbf{e}_{\parallel \mathbf{Q}}^{(\eta, \alpha)} \cdot \tilde{\nabla}_{\mathbf{r}_{\alpha l}} \rho(\mathbf{r}')$ denotes the dot-product of the in-plane components of these vectors. In the following, we shall denote by $\mathbf{R}_{\alpha l}$ and \mathbf{R}_l the in-plane components of $\mathbf{r}_{\alpha l}$ and \mathbf{r}_l , respectively.

Using this expression and the Bloch form of the wave-

functions, the Hartree-only component of the DFT matrix element given by Eq. (6) is approximately:

$$\begin{aligned} \langle \mathbf{K}', n' | \delta E_H^{(\eta)} | \mathbf{K}, n \rangle &\approx \sum_{\mathbf{g}' \mathbf{g}} u_{\mathbf{K}', \mathbf{g}'}^{(n')*} u_{\mathbf{K}, \mathbf{g}}^{(n)} \frac{1}{\Omega} \int d\mathbf{R} e^{i(\mathbf{K}' - \mathbf{K} + \mathbf{G}' - \mathbf{G} + \mathbf{Q}') \cdot \mathbf{R}} \int dz e^{i(g'_z - g_z)z} \\ &\times \sum_{\alpha l \mathbf{Q} \mathbf{Q}'} A_{\mathbf{Q}}^{(\eta, \alpha)} e^{i(\mathbf{Q} - \mathbf{Q}') \cdot \mathbf{R}_l} e^{i(\mathbf{Q} - \mathbf{Q}') \cdot \boldsymbol{\tau}_\alpha} e_{\parallel, \mathbf{Q}}^{(\eta, \alpha)} \cdot \int d\mathbf{R}' e^{-i\mathbf{Q}' \cdot (\mathbf{R}' - \mathbf{R}_{\alpha l})} \int dz' G_{\mathbf{Q}'}^{(0)}(z, z') \tilde{\nabla}_{\mathbf{R}_{\alpha l}} \rho(\mathbf{R}', z'), \end{aligned} \quad (10)$$

having expressed $G^{(0)}(\mathbf{r}, \mathbf{r}')$ in terms of its in-plane Fourier components.

In this expression, the factor

$$\sum_{\alpha} e^{i(\mathbf{Q} - \mathbf{Q}') \cdot \boldsymbol{\tau}_\alpha} \int d\mathbf{R}' e^{-i\mathbf{Q}' \cdot (\mathbf{R}' - \mathbf{R}_{\alpha l})} \times \int dz' G_{\mathbf{Q}'}^{(0)}(z, z') \tilde{\nabla}_{\mathbf{R}_{\alpha l}} \rho(\mathbf{R}', z') \quad (11)$$

does not depend on the cell index l thanks to the periodicity of the 2D crystal, so the factor $\sum_l e^{i(\mathbf{Q} - \mathbf{Q}') \cdot \mathbf{R}_l}$ appearing in Eq. (10) is nonzero only when $\mathbf{Q} = \mathbf{Q}'$, up to a vector of the reciprocal lattice (which ultimately will be ignored).

Since dielectric screening – whose effects we are considering here – is particularly strong at long wavelengths, much longer than the thickness of the TMD monolayer, we can consider the change of the charge $\tilde{\nabla}_{\mathbf{R}_{\alpha l}} \rho(\mathbf{R}', z')$ as localized at $z' = d$ (so, is proportional to $\delta(z' - d)$). Thus, the term given by Eq. (11) can be approximated by:

$$\begin{aligned} \sum_{\alpha} e^{-i\mathbf{Q}' \cdot \boldsymbol{\tau}_\alpha} \int d\mathbf{R}' e^{i\mathbf{Q}' \cdot (\mathbf{R}' - \mathbf{R}_l)} G_{\mathbf{Q}'}^{(0)}(z, d) \tilde{\nabla}_{\mathbf{R}_{\alpha l}} \rho(\mathbf{R}', d) \\ = G_{\mathbf{Q}'}^{(0)}(z, d) \sum_{\alpha} e^{-i\mathbf{Q}' \cdot \boldsymbol{\tau}_\alpha} [\tilde{\nabla}_{\boldsymbol{\tau}_\alpha} \rho]_{\mathbf{Q}'} \end{aligned} \quad (12)$$

having selected the cell $\mathbf{R}_l = 0$ (without loss of generality for the argument given above regarding the independence of Eq. (11) on the cell index l) and having defined the 2D Fourier components:

$$[\tilde{\nabla}_{\boldsymbol{\tau}_\alpha} \rho]_{\mathbf{Q}} = \int d\mathbf{R} e^{i\mathbf{Q} \cdot \mathbf{R}} \tilde{\nabla}_{\boldsymbol{\tau}_\alpha} \rho(\mathbf{R}, d). \quad (13)$$

Finally, assuming that the Green's function $G_{\mathbf{Q}}^{(0)}(z, d)$ is constant over the 'vertical' support of the wavefunctions (a good approximation especially in the important region of small Q), Eq. (10) becomes:

$$\begin{aligned} \langle \mathbf{K}', n' | \delta E_H^{(\eta)} | \mathbf{K}, n \rangle &\approx \sum_{\mathbf{g}' \mathbf{g} \mathbf{Q}} \delta_{\mathbf{K}' - \mathbf{K} + \mathbf{G}' - \mathbf{G}, \mathbf{Q}} \delta_{g'_z, g_z} u_{\mathbf{K}', \mathbf{g}'}^{(n')*} u_{\mathbf{K}, \mathbf{g}}^{(n)} \\ &\times \sum_{\alpha} e^{-i\mathbf{Q} \cdot \boldsymbol{\tau}_\alpha} A_{\mathbf{Q}}^{(\eta)} e_{\mathbf{Q}}^{(\eta, \alpha)} \cdot \tilde{\nabla}_{\boldsymbol{\tau}_\alpha} \rho(\mathbf{Q}) G_{\mathbf{Q}}^{(\text{vac})}(d, d). \end{aligned} \quad (14)$$

Here, the Green's function $G_{\mathbf{Q}}^{(0)}(z, z') = e^{-Q|z - z'|} / (2\epsilon_0 Q)$ has been replaced by the Green's function, $G_{\mathbf{Q}}^{(\text{vac})}(z, z')$, of a system consisting of a 2D layer of dielectric constant $\epsilon_{2D}^{(\infty)}$ and thickness h . This may better mimic the geometry implicitly used in DFT calculations. We have also assumed that $G^{(\text{vac})}$ is almost constant over the thickness of the 2D layer (once more, a good approximation for sufficiently small Q , the region in which screening is most effective):

$$G_{\mathbf{Q}}^{(\text{vac})}(d, d) = \frac{1}{2\epsilon_{2D}^{(\infty)} Q} \mathcal{G}_{\mathbf{Q}}^{(\text{vac})}(d, d), \quad (15)$$

with:

$$\mathcal{G}_{\mathbf{Q}}^{(\text{vac})}(d, d) = 1 + 2\lambda e^{-Qh} \frac{\lambda e^{-Qh} - 1}{1 - \lambda^2 e^{-2Qh}}, \quad (16)$$

and

$$\lambda = \frac{\epsilon_{\text{vac}} - \epsilon_{2D}^{(\infty)}}{\epsilon_{\text{vac}} + \epsilon_{2D}^{(\infty)}}. \quad (17)$$

We have made use of the assumed homogeneity and isotropy of the system on the (x, y) plane, to express these Green's function as dependent only on the magnitude Q of \mathbf{Q} .

To summarize, assuming:

1. that the Hartree component dominates;
2. that for in-plane phonons the ionic displacement lies purely on the plane of the 2D crystal;
3. that the change of the charge caused by this displacement is localized at $z' = d = h/2$;
4. and that the Poisson Green's function is constant over the effective thickness h of the 2D layer,

then, the electron-phonon matrix element can be written as:

$$\begin{aligned} \langle \mathbf{K} + \mathbf{Q}, n' | \delta E_H^{(\eta)} | \mathbf{K}, n \rangle &\approx \sum_{\mathbf{g} \mathbf{g}'} u_{\mathbf{K} + \mathbf{Q}, \mathbf{g}'}^{(n')*} u_{\mathbf{K}, \mathbf{g}}^{(n)} \sum_{\alpha} e^{-i\mathbf{Q} \cdot \boldsymbol{\tau}_\alpha} \\ &\times A_{\mathbf{Q}}^{(\eta, \alpha)} e_{\mathbf{Q}}^{(\eta, \alpha)} \cdot \tilde{\nabla}_{\boldsymbol{\tau}_\alpha} \rho(\mathbf{Q}) G_{\mathbf{Q}}^{(\text{vac})}(d, d), \end{aligned} \quad (18)$$

having ignored *Umklapp* contributions (that is, having replaced $\mathbf{Q} + \mathbf{G} - \mathbf{G}'$ by \mathbf{Q}), since the Poisson Green's function $G_{\mathbf{Q}}^{(\text{vac})}(d, d)$ decays quickly with Q .

The important result of this long discussion is that, for a given wave vector \mathbf{Q} , the matrix element depends linearly on the Poisson Green's function $G_{\mathbf{Q}}^{(\text{vac})}(d, d)$. Therefore, to estimate the matrix elements in the dielectric environment described above in Sec. II A, we may simply replace the 'vacuum' Poisson Green's function $G_{\mathbf{Q}}^{(\text{vac})}(d, d)$ with the Green's function for the Poisson equation with the boundary conditions dictated by the double-gate geometry of Sec. II A. This can be calculated using trivial but cumbersome algebra and, for the general double-gate geometry, $G_{\mathbf{Q},\omega}^{(\text{env})}(d, d)$ is given by:

$$G_{\mathbf{Q},\omega}^{(\text{env})}(d, d) = \frac{1}{2\epsilon_{2D}(Q, \omega)Q} \mathcal{G}_{Q,\omega}^{(\text{env})}(d, d), \quad (19)$$

where:

$$\mathcal{G}_{Q,\omega}^{(\text{env})}(d, d) = \frac{1}{1 + e^{-Qh} \frac{2\lambda_b(Q, \omega)\lambda_t(Q, \omega)e^{-Qh} - \lambda_b(Q, \omega) - \lambda_t(Q, \omega)}{1 - \lambda_b(Q, \omega)\lambda_t(Q, \omega)e^{-2Qh}}}. \quad (20)$$

The quantities $\lambda_b(Q, \omega)$ and $\lambda_t(Q, \omega)$ are given by:

$$\lambda_b(Q, \omega) = \frac{\epsilon_{\text{box}}(\omega) \coth(Q, t_b) - \epsilon_{2D}(Q, \omega)}{\epsilon_{\text{box}}(\omega) \coth(Q, t_b) + \epsilon_{2D}(Q, \omega)}, \quad (21)$$

$$\lambda_t(Q, \omega) = \frac{\epsilon_{\text{tox}}(\omega) \coth(Q, t_t) - \epsilon_{2D}(Q, \omega)}{\epsilon_{\text{tox}}(\omega) \coth(Q, t_t) + \epsilon_{2D}(Q, \omega)}, \quad (22)$$

with $\epsilon_{\text{box}}(\omega)$ and $\epsilon_{\text{tox}}(\omega)$ given by Eqs. (1) and (2) and $\epsilon_{2D}(Q, \omega)$ given by Eq. (3) (or Eq. (4) in the simpler small- Q approximation). Therefore, for a given scattering process involving a phonon of branch η and wave vector \mathbf{Q} , we can account for the presence of the different dielectric environment and free-carrier screening by simply rescaling the scattering rates calculated using DFT/EPW by the squared ratio:

$$\left| \frac{\mathcal{G}_{Q,\omega_Q^{(\eta)}}^{(\text{env})}(d, d)}{\mathcal{G}_Q^{(\text{vac})}(d, d)} \right|^2. \quad (23)$$

This can be easily implemented in Monte Carlo simulations: We use the 'bare' scattering rates computed for free-standing layers but, after a collision involving

a TMD phonon with wave vector \mathbf{Q} and frequency $\omega_Q^{(\eta)}$, we accept or reject the collision with a probability distribution given by Eq. (23).

D. Electron-IPP scattering

1. Secular equation, IPP dispersion, and scattering potential for the double-gate geometry

In order to obtain the dispersion of the hybrid IPPs, we must first consider the potential associated with these excitations. Here we follow the procedure described in Ref. [17] for the gate-insulator/Si-inversion-layer system and in Refs. [21] and [72] for supported graphene and supported and gated graphene, respectively. For the double-gate geometry described in Sec. II A, the potential has the form:

$$\phi_{Q,\omega}(z) = \begin{cases} ae^{Qz} + Ae^{-Qz} & (-t_b \leq z \leq 0) \\ be^{Qz} + de^{-Qz} & (0 < z \leq h) \\ de^{Qz} + fe^{-Qz} & (h < z \leq t_t + h) \end{cases} \quad (24)$$

Imposing the continuity of the components of the electric field, \mathbf{E}_{\parallel} , and of the displacement field, D_z , parallel and normal, respectively, to the plane of the interfaces, and setting $\phi_{Q,\omega}(-t_b) = \phi_{Q,\omega}(t_t + h) = 0$, as required by the presence of the metal gates, we obtain a linear system of 6 equations in 6 unknowns (A, a, b, c, d , and f) that admits a nontrivial solution only if the determinant of the coefficients vanishes. This leads to the secular equation (omitting for simplicity the dependence of the dielectric functions on Q and ω):

$$\epsilon_{2D}[(\hat{\epsilon}_{2D} - \hat{\epsilon}_{\text{box}})e^{-Qh} - (\hat{\epsilon}_{2D} + \hat{\epsilon}_{\text{box}})e^{Qh}] - \epsilon_{\text{tox}}[(\hat{\epsilon}_{2D} - \hat{\epsilon}_{\text{box}})e^{-Qh} - (\hat{\epsilon}_{2D} + \hat{\epsilon}_{\text{box}})e^{Qh} \coth(Qt_t)] = 0, \quad (25)$$

where $\hat{\epsilon}_{2D} = \epsilon_{2D} \sinh(Qt_b)$ and $\hat{\epsilon}_{\text{box}} = \epsilon_{\text{box}} \cosh(Qt_b)$. This is an algebraic equation of 8th degree in ω^2 whose 8 solutions for a fixed Q give the dispersion $\omega_Q^{(i)}$ (with $i = 1, 8$). Note that, with some straightforward but laborious algebra, this equation can be rewritten in a form that exhibits explicitly its symmetry under exchange of the top and bottom dielectrics:

$$\epsilon_{2D}^2 \tanh(Qt_b) \tanh(Qt_t) + \epsilon_{\text{box}} \epsilon_{\text{tox}} \tanh(Qh) + \epsilon_{2D} \epsilon_{\text{tox}} \tanh(Qt_b) + \epsilon_{2D} \epsilon_{\text{box}} \tanh(Qt_t) = 0. \quad (26)$$

Once the secular equation is solved, for each mode i , the potential that solves the homogeneous system can be expressed in terms of an arbitrary multiplication constant. Solving for a, b, c, d , and f in terms of A , we have:

$$a = A e^{-2Qt_b} \quad (27a)$$

$$b = A \frac{1}{2} \left[1 - e^{-2Qt_b} + \frac{\epsilon_{\text{box}}(\omega)}{\epsilon_{2\text{D}}(Q, \omega)} (1 + e^{-2Qt_b}) \right] \equiv A \mathcal{B}_{Q, \omega}, \quad (27b)$$

$$c = A \frac{1}{2} \left[1 - e^{-2Qt_b} - \frac{\epsilon_{\text{box}}(\omega)}{\epsilon_{2\text{D}}(Q, \omega)} (1 + e^{-2Qt_b}) \right] \equiv A \mathcal{C}_{Q, \omega}, \quad (27c)$$

$$d = A \frac{\epsilon_{2\text{D}}(Q, \omega)(1 - e^{-2Qt_b}) \sinh(Qh) + \epsilon_{\text{box}}(\omega)(1 + e^{-2Qt_b}) \cosh(Qh)}{\epsilon_{\text{tox}}(\omega)[e^{Qh} + e^{-Q(h-2t_t)}]} \equiv A \mathcal{D}_{Q, \omega}, \quad (27d)$$

$$f = A \frac{\epsilon_{2\text{D}}(Q, \omega)(1 - e^{-2Qt_b}) \sinh(Qh) + \epsilon_{\text{box}}(\omega)(1 + e^{-2Qt_b}) \cosh(Qh)}{\epsilon_{\text{tox}}(\omega)[e^{-Qh} + e^{Q(h-2t_t)}]} \equiv A \mathcal{F}_{Q, \omega}, \quad (27e)$$

having made use the secular equation to write the last two expressions. These equations define implicitly the functions $\mathcal{B}_{Q, \omega}, \dots, \mathcal{F}_{Q, \omega}$.

In order to determine the constant A (all-important, since it determines the overall strength of the interaction), one could quantize these excitations following the usual canonical quantization procedure and the magnitude of A would be determined by the canonical commutation rules. However, here we follow the simpler but equivalent procedure of Refs. [17, 21, 72], based on Stern and Ferrell [73]: For each hybrid mode i , we calculate the total energy of the field (time-averaged and including self-energy terms) in terms of A and set it equal to the ground-state energy $\hbar\omega^{(i)}/2$. However, in order to consider separately the contribution $\Phi^{(\alpha)}(\omega)$ due to each bare phonon α ($=$ TO1, TO2, TO3, TO4, or ZO, the

‘phonon content’ discussed below and in Refs. [17, 21, 74–76]), we consider separately the time-averaged energy $\langle W_{Q, \omega_Q^{(i)}}^{(\alpha)} \rangle$ due to each bare mode α and set it equal to a fraction $\Phi^{(\alpha)}(\omega_Q^{(i)})$ of the oscillator ground-state energy:

$$\begin{aligned} \frac{2}{\Omega} \langle W_{Q, \omega_Q^{(i)}}^{(\alpha)} \rangle &= \frac{1}{\Omega} \int_{-\infty}^{t_t} dz \rho_{Q, \omega_Q^{(i)}}(z) \phi_{Q, \omega_Q^{(i)}}^{(\alpha)}(z) \\ &= \frac{1}{2} \hbar\omega_Q^{(i)} \Phi^{(\alpha)}(\omega_Q^{(i)}), \end{aligned} \quad (28)$$

where Ω is the normalization area.

Proceeding as in Refs. [17, 21, 72] and taking as scattering potential the potential at $z = 0$, we obtain for the scattering strength relative to the content of the ‘bare’ phonon α of the hybrid mode i :

$$\left| \mathcal{A}_{Q, \omega_Q^{(i)}}^{(\alpha)} \right|^2 = \frac{\hbar\omega_Q^{(i)}}{2Q} (1 - e^{-2Qt_b})^2 \Phi^{(\alpha)}(\omega_Q^{(i)}) \left| \frac{1}{\epsilon_{\text{TOT}}^{(\alpha, \text{high})}(Q, \omega_Q^{(i)})} - \frac{1}{\epsilon_{\text{TOT}}^{(\alpha, \text{low})}(Q, \omega_Q^{(i)})} \right|. \quad (29)$$

where $\epsilon_{\text{TOT}}^{(\alpha, \text{low})}(Q, \omega)$ and $\epsilon_{\text{TOT}}^{(\alpha, \text{high})}(Q, \omega)$ are the ‘total’ dielectric functions of the system assuming that mode α responds fully (‘low’) or does not respond (‘high’). They are given by:

$$\begin{aligned} \epsilon_{\text{TOT}}(Q, \omega) &= [\widetilde{\epsilon}_{\text{box}}(\omega)(1 - e^{-2Qt_b}) - \widetilde{\epsilon}_{2\text{D}}(Q, \omega)(\mathcal{B}_{Q, \omega} - \mathcal{C}_{Q, \omega})] (1 - e^{-2Qt_b}) + \\ &[\widetilde{\epsilon}_{2\text{D}}(Q, \omega)(\mathcal{B}_{Q, \omega} e^{Qh} - \mathcal{C}_{Q, \omega} e^{-Qh}) - \widetilde{\epsilon}_{\text{tox}}(\omega)(\mathcal{D}_{Q, \omega} e^{Qh} - \mathcal{F}_{Q, \omega} e^{-Qh})] (\mathcal{B}_{Q, \omega} e^{Qh} + \mathcal{C}_{Q, \omega} e^{-Qh}). \end{aligned} \quad (30)$$

Here the functions $\widetilde{\epsilon}_{\text{box}}(\omega)$, $\widetilde{\epsilon}_{\text{tox}}(\omega)$, and $\widetilde{\epsilon}_{2\text{D}}(Q, \omega)$ are calculated considering the full response of phonon α (‘low’) or assuming that mode α does not respond (‘high’). This is done by setting $\omega = 0$ or $\omega \rightarrow \infty$, respectively, in the expression representing the contribution of phonon α to the polarizability. For example, if $\alpha =$ TO2 (the high-frequency phonon of the bottom oxide), we set:

$$\epsilon_{\text{box}}^{(\text{TO2, high/low})}(\omega) = \epsilon_{\text{box}}^{(\infty/\text{mid})} + [\epsilon_{\text{box}}^{(0)} - \epsilon_{\text{box}}^{(\text{mid})}] \frac{\omega_{\text{TO},1}^2}{\omega_{\text{TO},1}^2 - \omega^2}. \quad (31)$$

As mentioned above, the quantity $\Phi^{(\alpha)}(\omega_Q^{(i)})$ appearing in Eqs. (28) and (29) denotes the content of the (uncoupled) phonon mode α of the hybrid mode i . To obtain this quantity we follow Refs. [74–76], as described also in Ref. [17] and [21].

Equation (29) reflects the fact that we have chosen the potential at $z = 0$ as scattering potential. The full symmetry of the system when $t_b = t_t$ may be restored by using, instead, the potential at $z = d = h/2$. However, this would not result in any significant change in the long-wavelength limit, $Q < 1/d$, the range of wavelengths in

which the IPP potential is strongest. This is consistent with the approximations also made in Eqs. (37) below and we shall show in Sec. III B that our results confirm the validity of the long-wavelength approximation.

2. Landau damping

The entire discussion has been based so far on the assumption that all the decoupled excitations of interest, electrons/holes, plasmons, and phonons, are pure eigenstates of the total Hamiltonian of the system. Clearly, this ignores the fact that optical phonons decay into acoustic phonons via two-phonon [77] or many-phonon processes [78–81] with a rather short lifetime of the order of ps; that acoustic phonons also decay, although with a much longer lifetime (often more than hundreds of ns [78, 80], shorter – but still hundreds of ps – in MoS₂ monolayers [82]), in addition to decaying via electron-phonon interactions and scattering with boundaries/interfaces. Even more important is the fact that this assumption ignores also the decay of plasmons into single-particle excitations via Landau damping [83–87]. As discussed above (Sec. II A), for wave vectors \mathbf{Q} such that $E(K_F - Q) - E(K_F) \leq \hbar\omega_P(Q) \leq E(K_F + Q) - E(K_F)$ (assuming isotropic dispersions for electrons and plasmons), plasmons cease to exist as well-defined eigenstates of the Hamiltonian and decay into single particle excitations.

The approach followed by Hauber and Fahy [36] accounts for Landau damping correctly in the case of the plasmon/optical-phonon coupling in bulk polar semiconductors and of the bottom-insulator/MoS₂/top-insulator system (namely the vacuum/MoS₂/vacuum, hBN/MoS₂/hBN, HfO₂/MoS₂/SiO₂, and vacuum/MoS₂/SiO₂ stacks). They have expressed the scattering rate in terms of the imaginary part of the total dielectric function, as it follows from the fluctuation-dissipation theorem [88–91]. Such a procedure can become quite cumbersome in complicated geometries. Therefore, we have reverted to our ‘brute-force’ approximation used in the past [17], but improved following Hauber and Fahy’s suggestion: Rather than considering unscreened phonons in the Landau-damped (single-particle) region, $Q \geq Q_{LD}$ (where the Landau-damping cut-off wave vector, Q_{LD} , has been already defined implicitly in Eq. (5) as being such that $E(K_F + Q_{LD}) - E(K_F) = \hbar\omega_P(Q_{LD})$), we have replaced the dynamic long-wavelength term $1 - \omega_P(Q)^2/\omega^2$ in Eq. (4) with the static Thomas-Fermi expression $1 + Q_{TF}^2/Q^2$. We denote by Q_{TF} the screening wave vector given by:

$$Q_{TF} = \frac{e^2 n}{2\epsilon_{2D,v} k_B T}, \quad (32)$$

in the non-degenerate limit (n is carrier density), or

$$Q_{TF} = \frac{e^2 m^* g}{2\pi \hbar^2 \epsilon_{2D,v}}, \quad (33)$$

in the degenerate limit (g is the valley degeneracy). This accounts approximately for the static response of the free carriers when the frequency of the perturbation is smaller than the plasma frequency; that is, when $\omega_P(Q) \gg \omega_Q^{(i)}$. In this region of wavelengths, the resulting secular equation yields only phonon-like branches, 6 of them in the DG geometry we have considered, each of them screened statically by the 2DEG. However, as we have already stressed before, electrons couple only with the components of four of the ‘bare’ modes, since the contribution to the due to the two modes arising from the TMD ZO phonons at the top and bottom interfaces is anti-symmetric [59], so that its matrix elements vanish in mirror-symmetric (σ_h -symmetric) monolayers [92].

3. Electron-IPP scattering rates

From Eqs. (24), (27a)-(27e), and (29), the IPP scattering potential needed to calculate the scattering rates has the form:

$$\phi_{Q,\omega}(\mathbf{r}) = e^{i\mathbf{Q}\cdot\mathbf{R}} \mathcal{A}_{Q,\omega} \times \begin{cases} e^{-2Qz} e^{Qz} + e^{-Qz} & (-t_b < z \leq 0) \\ \mathcal{B}_{Q,\omega} e^{Qz} + \mathcal{C}_{Q,\omega} e^{-Qz} & (0 < z \leq h) \\ \mathcal{D}_{Q,\omega} e^{Qz} + \mathcal{F}_{Q,\omega} e^{-Qz} & (h < z \leq t_t) \end{cases}. \quad (34)$$

Using Fermi’s golden rule, the scattering rate for an electron or hole in band n and 2D wave vector \mathbf{K} to emit or absorb a hybrid excitation of mode i with wave vector \mathbf{Q} and frequency $\omega_Q^{(i)}$ can be written as:

$$\frac{1}{\tau_n^{(i)}(\mathbf{K})} \approx \frac{2\pi}{\hbar} \sum_{n'\mathbf{K}'\mathbf{Q}} \left| \int_{\Omega} d\mathbf{r} \psi_{n'\mathbf{K}'}^*(\mathbf{r}) e \phi_{Q,\omega_Q^{(i)}}(\mathbf{r}) \psi_{n\mathbf{K}}(\mathbf{r}) \right|^2 \times \left\{ \begin{array}{l} N[\omega_Q^{(i)}] \\ 1 + N[\omega_Q^{(i)}] \end{array} \right\} \delta(E_{n\mathbf{K}} - E_{n'\mathbf{K}'} \pm \hbar\omega_Q^{(i)}), \quad (35)$$

where Ω is the normalization area and $N(\omega)$ is the equilibrium Bose-Einstein distribution function. The upper/lower term refers to absorption/emission of each hybrid mode. Using the Bloch form of the wavefunctions, $\psi_{n\mathbf{K}}(\mathbf{r}) = e^{i\mathbf{K}\cdot\mathbf{R}} u_{\mathbf{K}}^{(n)}(\mathbf{r})/\Omega^{1/2}$, we can rewrite the matrix element appearing in this expression as:

$$\frac{1}{\Omega} \int_{\Omega} d\mathbf{r} u_{\mathbf{K}'}^{(n')*}(\mathbf{r}) e^{i\mathbf{K}'\cdot\mathbf{R}} e \phi_{Q,\omega_Q^{(i)}}(z) e^{i\mathbf{Q}\cdot\mathbf{R}} u_{\mathbf{K}}^{(n)}(\mathbf{r}) e^{i\mathbf{K}\cdot\mathbf{R}}. \quad (36)$$

As we have already mentioned, in principle the Bloch functions and their energy $E_{n,\mathbf{k}}$ depend on the 3D wave

vector $\mathbf{k} = (\mathbf{K}, k_z)$. However, we ignore the dependence of $E_{n,\mathbf{k}}$ and $\psi_{n,\mathbf{K}}(\mathbf{r})$ on the out-of-plane component of the wave vector, k_z and also assume (as it would be correct only in the limit $h \rightarrow 0$) that the wavefunctions are localized on the plane of the 2D layer, so that $u_{\mathbf{K}}^{(n)}(\mathbf{r}) \approx U_{\mathbf{K}}^{(n)}(\mathbf{R})\delta(z)$, and Eq. (36) becomes:

$$\frac{1}{\Omega} e\mathcal{A}_{Q,\omega_Q^{(i)}} \int_{\Omega} d\mathbf{R} U_{\mathbf{K}'}^{(n')*}(\mathbf{R}) U_{\mathbf{K}}^{(n)}(\mathbf{R}) e^{i(\mathbf{K}-\mathbf{K}'+\mathbf{Q})\cdot\mathbf{R}}. \quad (37)$$

With the exception of the matrix element for the interaction with the ZO phonon-component of the potential, following the results of Ref. [59], treating the TMD wavefunctions as delta-functions, $\delta(z-d)$, should be a reasonable approximation also when assuming a non-zero thickness, but assuming a constant potential (along the out-plane direction z) in the 2D layer and wavefunctions similarly constant in the layers and zero outside the layer. At small Q , only intravalley scattering occurs and, in this case, the only error originates from ignoring the overlap integral between the initial and final states. For intraval-

ley processes, this is a minor effect. On the contrary, it may be an important effect for intervalley processes that may occur at large Q . However, in this case the scattering rate is small, because of the $1/Q$ dependence of the squared matrix elements.

Following the ‘usual’ procedure (see Eqs. (12.3)-(12.9) of Ref. [93]), setting $\mathbf{R} = \mathbf{R}_l + \mathbf{x}$ where \mathbf{R}_l are the lattice vectors and \mathbf{x} spans a unit cell, splitting the integral over the entire volume into a sum over cells times an integral over a single cell with area Ω_{cell} , this becomes:

$$\sum_{\mathbf{G}} e\mathcal{A}_{|\mathbf{Q}+\mathbf{G}|,\omega_Q^{(i)}} \delta^{(2)}(\mathbf{K}-\mathbf{K}'+\mathbf{Q}) \times \frac{1}{\Omega_{\text{cell}}} \int d\mathbf{x} U_{\mathbf{K}'}^{(n')*}(\mathbf{x}) U_{\mathbf{K}}^{(n)}(\mathbf{x}) e^{i\mathbf{G}\cdot\mathbf{x}}. \quad (38)$$

Finally, assuming that the overlap integral between the initial and final Bloch functions is unity (that is, ignoring ‘overlap-factor’ effects, usually negligible when \mathbf{K} and \mathbf{K}' differ only by a small wave vector \mathbf{Q}), ignoring *Umklapp* processes, thanks to the dependence of the matrix element on $1/Q$, in the infinite-volume normalization we finally have:

$$\frac{1}{\tau_n^{(i)}(\mathbf{K})} \approx \frac{2\pi}{\hbar} \sum_{n'\alpha} \int \frac{d\mathbf{Q}}{(2\pi)^2} \frac{e^2 \hbar \omega^{(i)}(Q)}{2Q} \Phi^{(\alpha)}[\omega^{(i)}(Q)] \left| \frac{1}{\epsilon_{\text{TOT}}^{(\alpha,\text{high})}[Q,\omega^{(i)}(Q)]} - \frac{1}{\epsilon_{\text{TOT}}^{(\alpha,\text{low})}[(Q,\omega^{(i)}(Q))]} \right| \times \left\{ \frac{N[\omega^{(i)}(Q)]}{1+N[\omega^{(i)}(Q)]} \right\} \delta[E_n(\mathbf{K}) - E_{n'}(\mathbf{K}+\mathbf{Q}) \pm \hbar\omega^{(i)}(Q)]. \quad (39)$$

It can be shown in general that the function $\epsilon_{\text{TOT}}(Q,\omega)$ defined by Eq. (30) (with the dielectric functions $\tilde{\epsilon}$ replaced by their normal expressions ϵ) is identical to the left-hand side of the secular equation, Eq. (25). Moreover, a little algebra shows that, in the limit $h \rightarrow 0$, Eq. (30) implies $\epsilon_{\text{TOT}}(Q,\omega) \rightarrow (1 - e^{-2Qt_b})^2 [\epsilon_{\text{box}}(\omega) \coth(Qt_b) + \epsilon_{\text{tox}}(\omega) \coth(Qt_t)]$ which, in turn, tends to $\epsilon_{\text{box}}(\omega) + \epsilon_{\text{tox}}(\omega)$ in the limit of infinitely thick insulators (that is, $t_b, t_t \rightarrow \infty$). These are the ‘usual’ expressions obtained in Refs. [12] and [21]. Therefore, in these latter limits, for a single interface between two dielectrics, we recover the usual expression for the ‘Fröhlich’ term inside the absolute value in Eq. (39):

$$\left| \frac{1}{\epsilon_{\text{box}}^{(\alpha,\text{high})}(Q,\omega_Q^{(i)}) + \epsilon_{\text{tox}}^{(\alpha,\text{high})}(Q,\omega_Q^{(i)})} - \frac{1}{\epsilon_{\text{box}}^{(\alpha,\text{low})}(Q,\omega_Q^{(i)}) + \epsilon_{\text{tox}}^{(\alpha,\text{low})}(Q,\omega_Q^{(i)})} \right|. \quad (40)$$

Explicit analytic calculations for a simple Si/SiO₂ system show that this expression yields the same scattering rates obtained by Hauber and Fahy [36] when accounting for a slightly different definition of $\epsilon_{\text{TOT}}(Q,\omega)$.

E. Full-band Monte Carlo simulations

The low-field carrier mobility has been calculated using the Monte Carlo method described in-detail in our previous work presented in Refs. [9, 65]. To provide here just the basic features of the numerical method, the band structure, scattering rates and phonon spectra discussed above are interpolated and tabulated on a fine \mathbf{k} -mesh, described in Sec. II B, that spans the entire Brillouin zone. As discussed in Refs. [1], [2], and [9], the extremely fine mesh we use, mentioned in Sec. II B (namely: a $201 \times 201 \times 1$ mesh covering a rectangular section that inscribes the triangular irreducible wedge of the hexagonal first Brillouin zone) is required to account correctly and accurately not only for energy conservation but also for the anisotropy and the strong nonparabolicity of the band structure around the conduction-band minimum (or minima) and valence-band maximum. (Additional details about the algorithms used in our numerical implementation of the Monte Carlo method are given in the ‘Supplemental material’ of Ref. [65].) A bilinear interpolation is used to obtain information at arbitrary points in the Brillouin zone. As already mentioned, scattering with the flexural acoustic and optical phonons (the out-of-plane ZAs and ZOs) is ignored, since the horizon-

TABLE II. Physical parameters used to calculate IPP scattering in the 2H TMD monolayers.

Parameter	MoS ₂	MoS ₂	MoTe ₂	WS ₂	WSe ₂	WTe ₂ ^d
$\hbar\omega_{ZO}$ (meV) ^a	34.2	20.14	28.17	35.6	20.51	14.6
t_{2D} (nm) ^b	0.612	0.649	0.71	0.612	0.648	0.422
$\epsilon^{(0)}(\epsilon_0)$ ^b	9.8	11.19	14.02	9.34	10.74	10.42
$\epsilon^{(\infty)}(\epsilon_0)$ ^b	9.69	10.99	13.24	9.24	10.64	10.32
$m_e^*(m_0)$ ^c	0.5	0.55	0.65	0.3	0.6	0.4
$m_h^*(m_0)$ ^c	0.6	0.62	0.95	0.4	0.35	0.5

^a From our DFT calculations

^b From Ref. [56]

^c Used only to compute $\omega_P(Q)$ and screening wavelength

^d See note [55]

tal mirror (σ_h) symmetry exhibited by the 2H TMDs we have considered forbids these interactions at first order. Second-order (two-phonon) processes, while important in graphene [94–98], are negligible in the materials of interest here [99]. The carrier mobility, μ , is extracted from the zero-field diffusion constant D via the Einstein relation, generalized in the case of degenerate TMDs, rather than from the velocity-field characteristics, since the former is less affected by stochastic noise [100]. The simulations are performed using a synchronous ensemble of 500 particles for simulation times of about 10 ps, as required to reach steady state and a sufficiently accurate statistics.

III. RESULTS AND DISCUSSION

In this section, we present our results – obtained using the full-band Monte Carlo method described above – regarding the effect of dielectric screening and IPP scattering on the transport properties of the double-gated monolayer TMD system discussed in Section II A. We discuss the carrier mobility in several supported and/or gated monolayer TMDs, all assumed to be supported by SiO₂. Examples of the band structure and phonon spectra for various TMDs considered here can be found in Ref. [9]. Table 3 of this reference lists also the all-important values of the energy separation between the conduction-band minima at the symmetry point K and the minima of the satellite Q-valleys obtained using the ONCV pseudopotentials and the GGA-PBE exchange-correlation functional.

Tables II and III list the physical parameters used in our calculations. The dielectric constant and layer thickness of monolayer TMDs are taken from Ref. [56]. The transverse optical (TO) phonon frequencies and the dielectric constant for the polar insulators are obtained from Ref. [17]. We have used the ‘effective’ dielectric constant for the polar insulators in our calculations, as suggested by [36].

TABLE III. Physical parameters of the polar insulators used to calculate IPP scattering.

Parameter	HfO ₂	SiO ₂	Al ₂ O ₃	AlN	h-BN	ZrO ₂
$\hbar\omega_{TO1}$ (meV) ^a	12.4	55.6	48.18	81.4	92.5	16.67
$\hbar\omega_{TO2}$ (meV) ^a	48.35	138.1	71.41	88.55	170.1	57.7
$\epsilon^{(0)}(\epsilon_0)$ ^a	22.0	3.9	12.53	9.14	5.1	24.0
$\epsilon^{(mid)}(\epsilon_0)$ ^a	6.58	3.05	7.27	7.35	4.45	7.75
$\epsilon^{(\infty)}(\epsilon_0)$ ^a	5.03	2.50	3.2	4.8	3.88	4.0
t_{ox} (nm) ^b	4.2	0.7	2.25	1.64	0.916	4.31

^a From Ref. [17]

^b Corresponding to an equivalent SiO₂ thickness of 0.7 nm. The top-insulator thickness was varied for some of the calculations shown in Sec. III B.

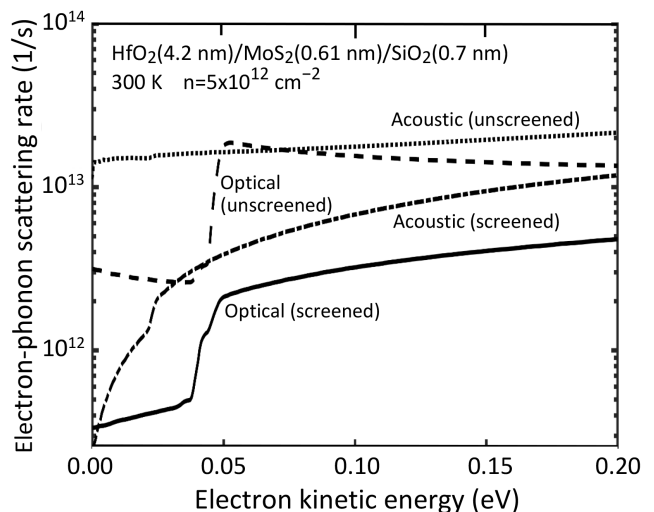


FIG. 2. Electron-phonon scattering rate in MoS₂ as a function of electron kinetic energy for the SiO₂/MoS₂/HfO₂ system accounting for the screening effects of the free carriers (assuming a sheet density of $5 \times 10^{12} \text{ cm}^{-2}$) and of the surrounding dielectrics while ignoring IPP scattering. For comparison, the unscreened ‘intrinsic’ electron-phonon scattering rates of MoS₂ are also shown. All rates have been averaged over equi-energy surfaces. The physical thickness of each layer is shown in parentheses in the legend.

A. Dielectric screening due to the insulators and free carriers

Before considering the effects of the all-important IPP scattering, we discuss first how the ‘intrinsic’ carrier mobility in the TMD monolayers (that is, limited only by scattering with the bulk TMD phonons) in the double-gate configuration is affected by the dielectric screening due to the free carriers in the TMD and the SiO₂ substrate/bottom-gate-insulator and various gate insulators, ignoring for now IPP scattering. The gate insulators we have considered range from the low- κ SiO₂ to the high- κ ZrO₂.

In Fig. 2 we compare the scattering rates for the unscreened electron/bulk phonons interaction in free-

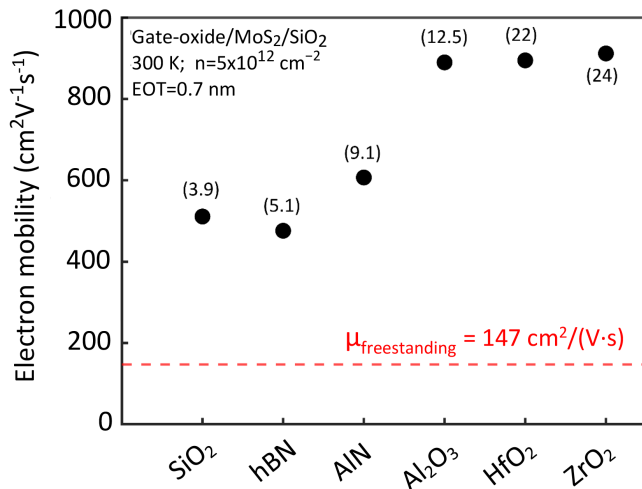


FIG. 3. Calculated 300 K electron mobility in the TMD channel of a gate-insulator/MoS₂/SiO₂ structure including only the effect of free-carrier and dielectric screening by the dielectrics (ordered with increasing static dielectric constant – shown in parentheses – from left to right), ignoring IPP scattering. The electron sheet-density in the TMD layer has been assumed to be $5 \times 10^{12} \text{ cm}^{-2}$.

standing MoS₂ with the screened rates for the same MoS₂ layer but embedded in a HfO₂/MoS₂/SiO₂ double-gate structure. The screened rates are more than one order of magnitude smaller than the unscreened rates, this difference being particularly large at low electron kinetic energies, since dielectric screening is most effective and long wavelengths and low-energy electrons can transfer only a small (crystal) momentum.

Such a reduction of the scattering rates results, obviously, in a much higher electron mobility in a layer embedded in double-gate structure than in the unscreened free-standing configuration, as shown in Fig. 3. For reference, the electron mobility of a free-standing MoS₂ monolayer without such ‘screening by the environment’, is $147 \text{ cm}^2/(\text{V.s})$ [9]. As expected, the mobility increases with increasing dielectric constant of the substrate. Screening by a HfO₂ and ZrO₂ gate insulator, the highest- κ dielectrics we consider, increases the phonon-limited electron mobility of MoS₂ by almost one order of magnitude, ($> 900 \text{ cm}^2/(\text{V.s})$). Even in the case of a SiO₂ gate oxide, one can see some modest gains, the electron mobility being enhanced to about $500 \text{ cm}^2/(\text{V.s})$. The beneficial effect caused by the presence of high- κ dielectrics has been observed experimentally [101–103] and theoretically explained both in the case of the impurity-limited electron mobility in MoS₂ [104] as well as of the phonon-limited mobility [103], although in this latter case the observed ‘phonon quenching’ and improvement of the mobility was attributed to HfO₂-induced tensile strain.

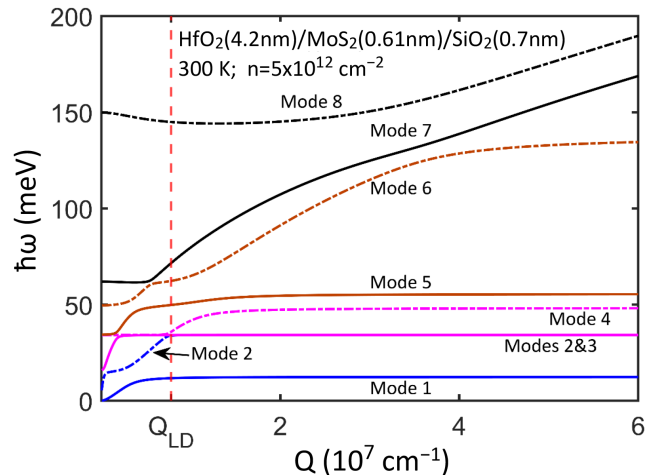


FIG. 4. Dispersion of the fully hybridized IPPs for the SiO₂/MoS₂/HfO₂ structure. The wave vector Q_{LD} ($\approx 7.8 \times 10^6 \text{ cm}^{-1}$ at the sheet density shown in the legend) indicates the wavelength-cutoff beyond which the plasmons are Landau-damped. For $Q > Q_{\text{LD}}$, only statically-screened SO phonons survive.

B. Electron-IPP scattering

As already anticipated, IPP scattering negates completely the benefits we have just discussed. In order to understand the nature of this scattering process, we first need to consider the dispersion of these hybrid modes. This is shown in Fig. 4 for the HfO₂/MoS₂/SiO₂ double-gate structure. These results have been obtained assuming an electron sheet-density of $5 \times 10^{12} \text{ cm}^{-2}$ and room and temperature (300 K) by solving the secular equation, Eq. 25 for each Q . This is an 8th-degree algebraic equation that we have solved using a combination of the Newton’s method, of the bisection technique, and by finding the eigenvalues of the ‘companion matrix’ associated to the polynomial appearing at the left-hand-side of Eq. (25) [105]. We must stress again that, as explained in sec IID 2, we consider the full dispersion relation shown in this figure only for $Q \leq Q_{\text{LD}}$.

In the case considered in Fig. 4, we can see clearly the full hybridization of the modes, especially around $Q \sim 1/\text{nm}$. Only at large Q do the modes become almost pure plasmon- or phonon-like excitations. In particular, the label ‘mode 1’ refers to the lowest-energy IPP that is mainly a 2D plasmon at small Q and becomes mainly the low-frequency TO phonon of HfO₂ at large Q . Similarly, at large Q , modes 2-5 originate, respectively, mainly from the two antisymmetric interface MoS₂ (mostly ZO-like) interface phonons [59], from the low-frequency SiO₂ and from the high-frequency HfO₂ phonons. In the same range of large Q , mode 6 originates mainly from the high-frequency SiO₂ TO phonon, whereas, finally, modes 7 and 8 represent mainly the 2D plasmons at the bottom (MoS₂/SiO₂) and top (MoS₂/HfO₂) interfaces.

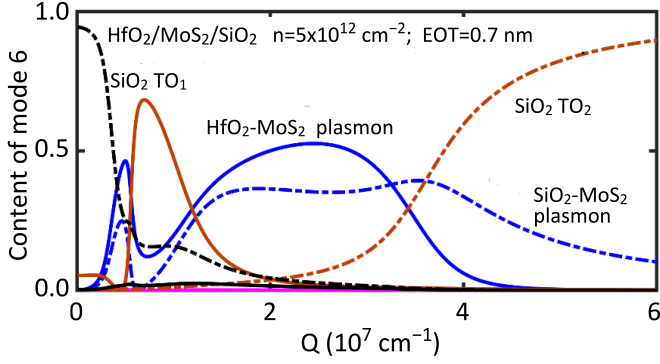


FIG. 5. Phonon and plasmon content of the fully hybridized IPP labeled ‘mode 6’ in Fig. 4.

An example of the complicated hybridization of these modes is illustrated in Fig. 5: The phonon, $\Phi_Q^{(\alpha)}(\omega_Q^{(5)})$, and plasmon content of the decoupled mode 6 shown in Fig. 4 is plotted as a function of wave vector Q . At small Q , this excitation is mainly a low-energy SiO_2 phonon (TO1); as its wavelength decreases, it hybridizes with the high-frequency HfO_2 phonon, with the MoS_2 optical phonon, with both MoS_2 interface plasmons (at the lower and upper interfaces), becoming mainly a high-frequency SiO_2 phonon as $Q \rightarrow \infty$. For $Q \approx 10^6/\text{cm}$, this mode hybridizes significantly with up to 5 different bare modes. As shown below, this is the long-wavelength, non Landau-damped region in which scattering with these modes controls electronic transport; therefore, this hybridization is an essential physical ingredient, as already shown in Refs. [17, 21, 72] for the case of supported and gated graphene.

For $Q > Q_{\text{LD}} (\approx 7.8 \times 10^6 \text{ cm}^{-1})$ in MoS_2 for an electron sheet density of $5 \times 10^{12} \text{ cm}^{-2}$), the 8 hybrid branches shown in Fig. 4 are replaced by six surface-phonon-like (SO) branches obtained by solving the secular equation, Eq. (25), but ignoring the plasma response of the 2DEG by replacing $(1 - \omega_P(Q)^2/\omega^2)$ in Eq. (4) with the static Thomas-Fermi expression, $1 + Q_{\text{TF}}^2/Q^2$ (where Q_{TF} is the screening wave vector given by Eqs. (32) and (33)).

Very important is Fig. 6 in which we show the electron-IPP scattering rates separately for interactions with the 8 long-wavelength, fully hybridized IPPs (Fig. 6(a)) and with the interface optical phonons (SOs) hybridized among themselves but decoupled from the Landau-damped 2D plasmons (Fig. 6(b)). These rates have been obtained integrating Eq. (39) only for values of the transfer wave vector Q smaller (Fig. 6(a)) or larger (Fig. 6(b)) than the Landau-damping cut-off Q_{LD} . As for the results of Fig. 4, the calculations have been performed assuming an electron sheet-density of $5 \times 10^{12} \text{ cm}^{-2}$ and room temperature (300 K). The results shown in this figure show that, despite the fact that Landau damping prevents plasmons to exist over a large region of momentum-space, nevertheless the $\sim 1/Q^2$ -behavior of the squared electron-IPP matrix elements causes scattering to be dominated processes involving Q -vectors of magnitude

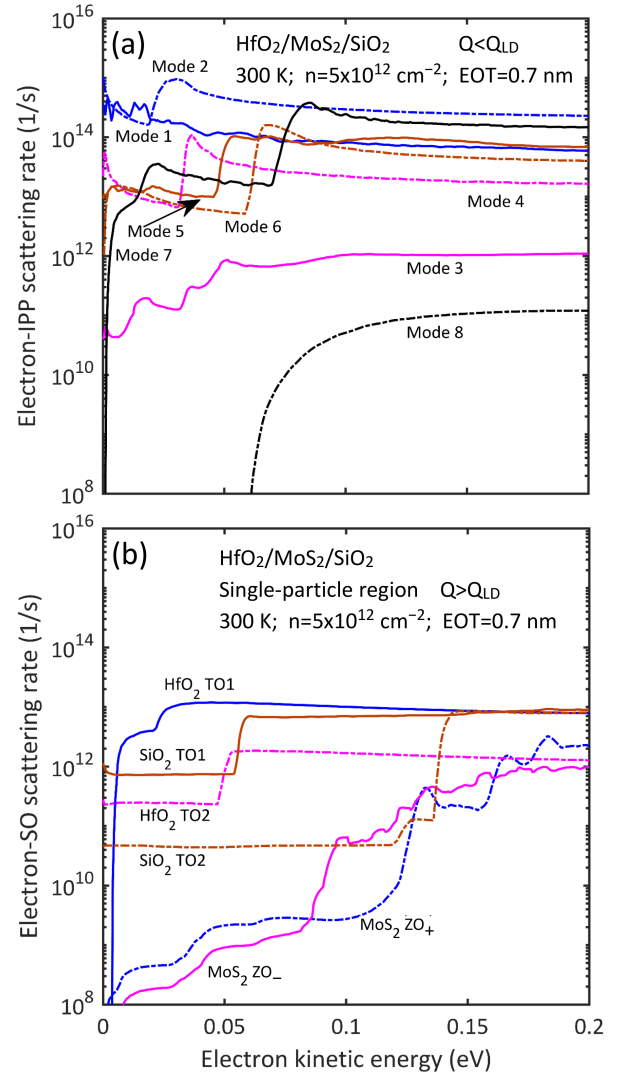


FIG. 6. Electron-IPP scattering rates *vs.* electron kinetic energy in the $\text{SiO}_2/\text{MoS}_2/\text{HfO}_2$ stack calculated for a carrier density of $5 \times 10^{12} \text{ electrons cm}^{-2}$ and at 300 K. The anisotropic rates – functions of the electron wave vector \mathbf{k} – have been averaged over equi-energy surfaces. The rates shown in the top frame, (a), have been computed considering only final states such that the wave vector transfer Q is smaller than the Landau-damping cutoff $Q_{\text{LD}} \approx 7.8 \times 10^6 \text{ cm}^{-1}$. They represent interactions only with the long-wavelength fully hybridized IPPs. The rates for scattering only with the short-wavelength SO modes (optical phonons hybridized among themselves but decoupled from the Landau-damped plasmons) are shown in the bottom frame, (b). A comparison with Fig. 4 permits the identification of the eight modes shown in frame (a).

small enough to render the role of phonon/plasmon coupling very important. Of course, such a small- Q scattering process results in momentum-relaxation rates that are not as strong as the scattering rates. Yet, coupling to plasmons is an effect that cannot be neglected. This also shows that, at the electron sheet-density of interest, considering the long-wavelength limit, $Q < Q_{\text{LD}} \approx$

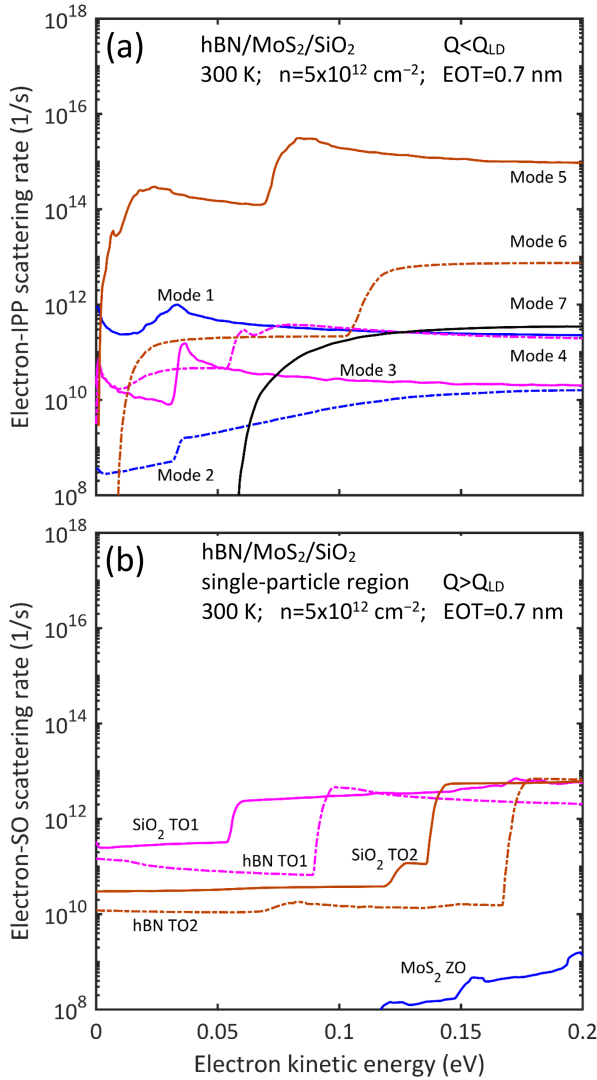


FIG. 7. As in Fig. 6, but for the SiO₂/MoS₂/hBN stack.

$10^6 - 10^7 \text{ cm}^{-1} \ll 2\pi/h \approx 10^8 \text{ cm}^{-1}$, appears to be a sensible approximation.

Both in the long-wavelength regime as well as in the single-particle region, transport is controlled by the HfO₂ phonons (modes 1 and 2) and, to some extent, by the low-frequency phonon of the SiO₂ substrate. Note that the scattering rates labeled ‘ZO_±’ in frame (b) refer to the interaction with the weak non-ZO-component of SO excitations at the top and bottom TMD/insulator interfaces, excitations that are mainly TMD optical flexural modes. A comparison of Fig. 7 with Fig. 6 shows how a low- κ gate-insulator, like hBN, induces negligible IPP scattering. Also in this case, electron-IPP scattering is dominated by the long-wavelength processes. However, the strongest scattering channel is due to the interaction with the SiO₂ phonons (see also Fig. 8), especially with the low-frequency mode at small electron energies.

We shall now discuss how IPP scattering affects the carrier mobility *i)* with different gate insulators, *ii)* as a function of their thickness, *iii)* of the dielec-

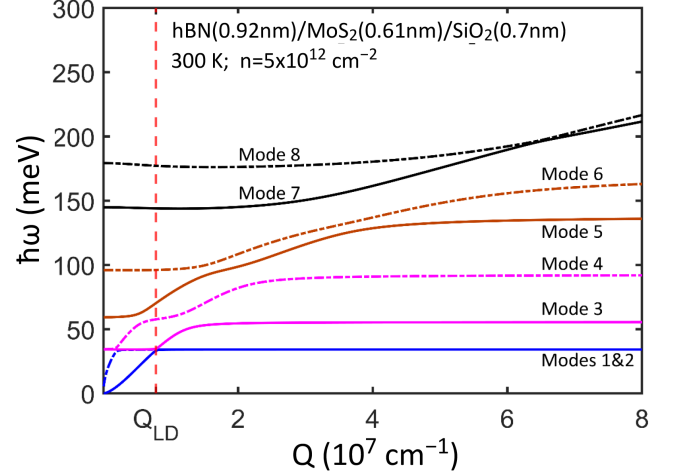


FIG. 8. Dispersion of the fully hybridized IPPs for the SiO₂/MoS₂/hBN structure.

TABLE IV. Calculated 300 K electron mobility (in $\text{cm}^2\text{V}^{-1}\text{s}^{-1}$) in TMD monolayers in a double-gate stack, assuming SiO₂ as bottom insulator and different gate insulators. Both insulators are assumed to have an equivalent oxide thickness (EOT) of 0.7 nm. The results have been obtained assuming a TMD electron sheet-density of $5 \times 10^{12} \text{ cm}^{-2}$.

System	MoS ₂	MoSe ₂	MoTe ₂	WS ₂	WSe ₂	WTe ₂ ^a
Freestanding	147	92	43	380	180	166
SiO ₂ /TMD/SiO ₂	76	65	41	141	96	87
hBN/TMD/SiO ₂	319	195	55	795	260	278
AlN/TMD/SiO ₂	51	83	36	65	79	53
Al ₂ O ₃ /TMD/SiO ₂	32	27	19	54	36	38
HfO ₂ /TMD/SiO ₂	43	16	28	69	39	51
ZrO ₂ /TMD/SiO ₂	34	13	20	35	24	25

^a See note [55]

tric constant assumed for the TMD monolayer, *iv)* of the density of the 2DEG, and, finally, *v)* on temperature.

i) Dependence on the gate insulator. In Fig. 9 we show the carrier mobility calculated in TMD monolayers assuming various top insulators, listed in order of increas-

TABLE V. Calculated 300 K hole mobility (in $\text{cm}^2\text{V}^{-1}\text{s}^{-1}$) in the TMD channel of several double-gate stacks, as in Table IV.

System	MoS ₂	MoSe ₂	MoTe ₂	WS ₂	WSe ₂	WTe ₂ ^a
Freestanding	49	74	295	152	179	169
SiO ₂ /TMD/SiO ₂	43	61	118	79	210	55
hBN/TMD/SiO ₂	68	102	363	202	396	268
AlN/TMD/SiO ₂	27	55	94	41	178	19
Al ₂ O ₃ /TMD/SiO ₂	19	19	44	33	45	15
HfO ₂ /TMD/SiO ₂	23	22	73	32	85	26
ZrO ₂ /TMD/SiO ₂	16	17	39	26	11	23

^a See note [55]

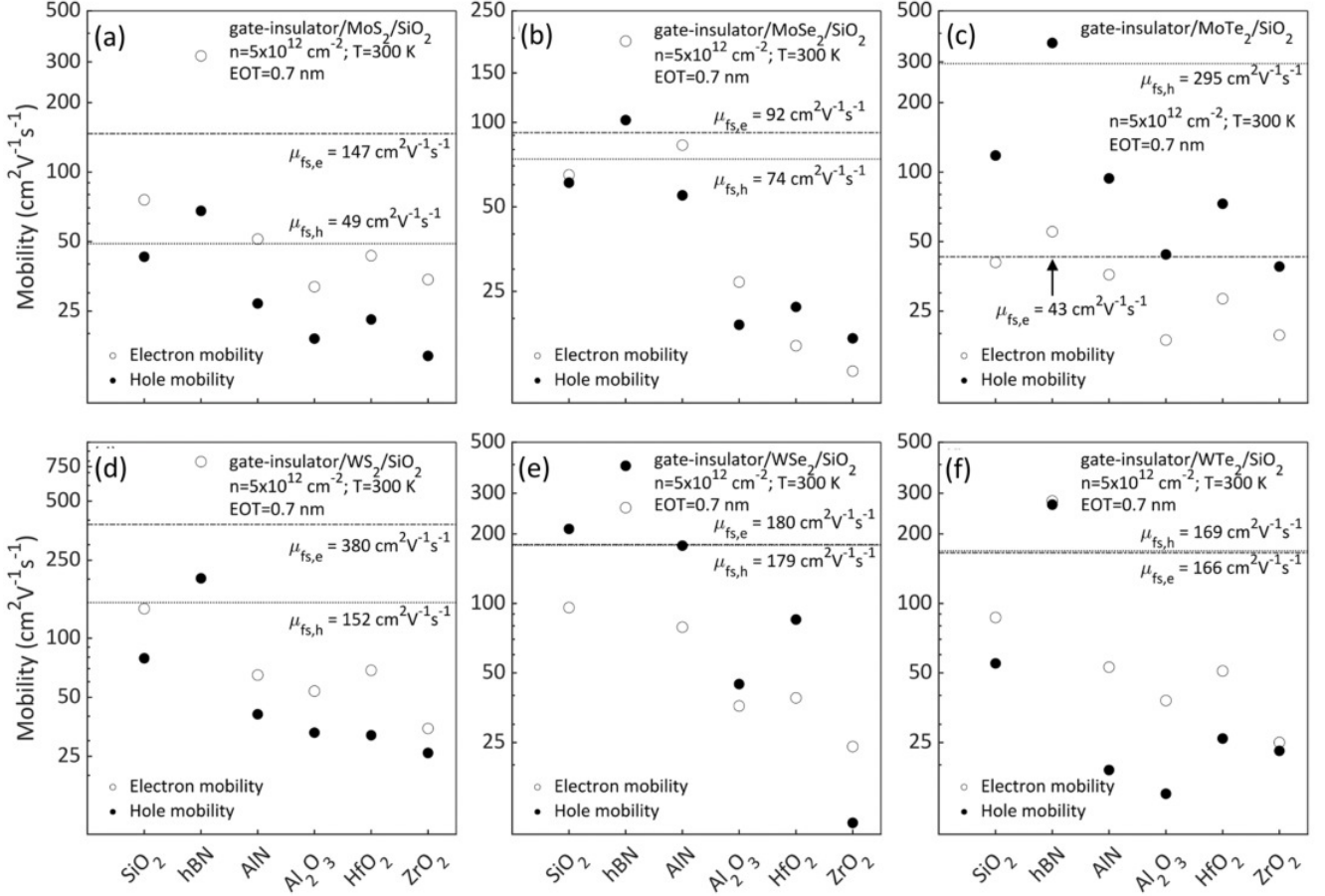


FIG. 9. (a): Calculated 300 K electron (open symbols) and hole mobility (solid symbols) in the TMD channel of a gate-insulator/MoS₂/SiO₂ structure with different gate insulators (ordered with increasing static dielectric constant – shown in parentheses – from left to right). Note that the mobility generally decreases as the static dielectric constant of the gate insulator increases, but phonon resonances cause ‘dips’ in the cases of Al₂O₃ and, to a smaller extent, ZrO₂. Moreover, the absence of low-energy phonons in hBN results in a mobility larger than in free-standing MoS₂ (shown by the horizontal lines), thanks to the beneficial effect of dielectric screening of the bulk phonons by high- κ insulators. (b): The same, but for the gate-insulator/MoSe₂/SiO₂ structure and (c), for the gate-insulator/MoTe₂/SiO₂ structure. One can notice a similar behavior. Finally, frames (d), (e) and (f) shows the same information for the gate-insulator/WS₂/SiO₂, gate-insulator/WSe₂/SiO₂, and gate-insulator/WTe₂/SiO₂ systems, respectively. In all cases, the carrier sheet density in the TMD layers has been assumed to be $5 \times 10^{12} \text{ cm}^{-2}$.

ing dielectric constant, from SiO₂ to ZrO₂, for the double-gate structure we have considered, assuming SiO₂ as substrate. Also in this case, we have assumed a carrier sheet-density of $5 \times 10^{12} \text{ cm}^{-2}$ and room temperature. For convenience, we list the calculated values also in Tables IV and V

Among the various supported and gated TMDs considered, the best electron mobility, $795 \text{ cm}^2/(\text{V}\cdot\text{s})$, is obtained for the SiO₂/WS₂/hBN system. An excellent hole mobility, $396 \text{ cm}^2/(\text{V}\cdot\text{s})$ is also predicted for the SiO₂/WSe₂/hBN stack. These results confirm the general trend observed previously for MoS₂ [106]: The carrier mobility decreases almost monotonically with increasing dielectric constant of the gate insulator, with two exceptions: **1**. The beneficial effects of dielectric screening of the ‘out-of-plane’ field lines are seen for hBN, since electron-IPP scattering is weak in this case,

thanks to its relatively low ionic polarization and the high phonon frequencies resulting from the light weight of the B and N ions. A similar result has been obtained by Ma and Jena [33]. **2**. On the contrary, resonance effects among the optical phonons of the substrate, of the TMD layer, and of the top insulator result in a low carrier mobility when AlN and/or Al₂O₃ are taken as gate insulators. In particular, looking at Fig. 9(a), one notices that the calculated 300 K electron and hole mobilities in SiO₂-supported monolayer MoS₂ decrease as the gate insulator is changed from hBN to HfO₂, but it reaches a particularly high value for hBN and a very low value for Al₂O₃. A similar behavior, although to a different extent, can be seen also for most of the other cases shown in Fig. 9. In all cases, hBN exhibits the best mobility, even higher than what we have calculated in free-standing monolayers, as explained above.

Obviously, this comes at the price of the relatively low dielectric constant – that defies the very reason behind the use of high- κ insulators, as dictated by scaling laws – and a relatively small potential barrier at the channel-insulator interface – that would lead to a large gate-leakage current if hBN were to be used as the sole gate dielectric.

The role of resonances. The low mobility seen for Al_2O_3 and ZrO_2 in almost all cases is caused by fact that the low-frequency optical phonon of Al_2O_3 (or high-frequency ZrO_2 TO phonon) oscillates at a frequency that is very close to the frequency of the low-energy SiO_2 TO phonons and of the hybridized MoS_2 ZO phonon. In these cases, these modes couple very strongly and, as a result of this resonance, the large interface polarization-charge strengthens the IPP scattering potential. A similar effect has been already predicted theoretically for the $\text{Si}/\text{SiO}_2/\text{poly-Si}$ -gate system. When the poly-Si density yields a plasma frequency close to the TO-frequency of SiO_2 , the resonance of these two modes causes a low carrier mobility (Refs. [52–54]). Obviously, one concern about the accuracy of these results stems from the consideration that such an effect is extremely sensitive to the phonon frequencies chosen for the calculations (approximated from the broad peaks seen by Fourier-transform infrared spectroscopy, FTIR [17], for example) and observed in dielectrics used in experiments (whose morphology and composition may or may not be stoichiometric and amorphous/polycrystalline). Small changes of the phonon frequency may result in significantly different values for the mobility.

ii) Dependence on insulator thickness. Figure 10 shows the dependence of the carrier mobility – in the same double-gate systems – on the thickness of the gate insulator. As a general trend, we observe that the mobility decreases as the thickness of the insulator increases. This is due to the screening of the IPP scattering-potential due to the proximity of an ideal metal gate. In the $\text{HfO}_2/\text{MoS}_2/\text{SiO}_2$ system, we see a 20% increase of the mobility when the equivalent- SiO_2 oxide thickness (EOT) decreases from 1.2 to 0.7 nm. A similar trend is seen in the $\text{HfO}_2/\text{WS}_2/\text{SiO}_2$ stack, although the effect is stronger. This is due to the fact that the electron mobility in free-standing WS_2 is larger than in MoS_2 , so that the mobility is much more sensitive to any changes of the strength of IPP scattering.

iii) Dependence on the dielectric constant of the TMD monolayer. All values given so far for the carrier mobility have been obtained using the ‘effective’ static and optical dielectric constants for the TMD layers. However, given the anisotropy of the dielectric constant of the TMD layers and the various approximations used in the literature and here, it is interesting to see how the mobility varies as this parameter is changed. For

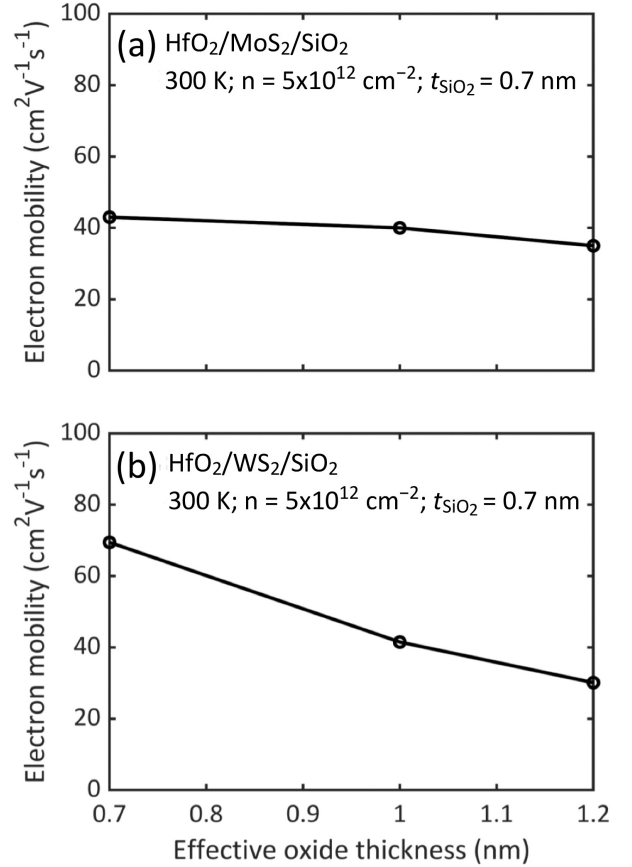


FIG. 10. (a): Calculated 300 K electron mobility in the TMD channel of a $\text{HfO}_2/\text{MoS}_2/\text{SiO}_2$ structure with a different thickness of the gate insulator; (b): The same, but for the $\text{HfO}_2/\text{WS}_2/\text{SiO}_2$ structure. A carrier sheet density of $5 \times 10^{12} \text{ cm}^{-2}$ has been assumed in these calculations. The symbols represent calculated data, the lines are only a guide to the eye.

MoS_2 , for example, the static and the high-frequency out-of-plane dielectric constants are $6.2\epsilon_0$ and $6.1\epsilon_0$ (Ref. [56]), respectively; the effective and geometric-averaged static(optical) values are $9.8(9.69)\epsilon_0$, and $11.42(11.31)\epsilon_0$. As a trend, the electron mobility increases with increasing TMD dielectric constant. In particular, for the $\text{HfO}_2/\text{MoS}_2/\text{SiO}_2$ stack, the mobility obtained using the out-plane dielectric constant is about $38 \text{ cm}^2\text{V}^{-1}\text{s}^{-1}$. This value increases by approximately 20%, to $43 \text{ cm}^2\text{V}^{-1}\text{s}^{-1}$ when using the effective dielectric constant, and by almost 60% (to $58 \text{ cm}^2\text{V}^{-1}\text{s}^{-1}$) when using the geometric average for the dielectric constant. Such a trend, also reported by Hauber and Fahy [36], is just due to the expected role of dielectric screening.

iv) Dependence on carrier density. In Fig. 11, looking at the variation of mobility with varying free-electron density, we observe only a marginal improvement when the density increase from 10^{11} cm^{-2} to 10^{13} cm^{-2} . Since the free carriers are confined in the 2D plane of the layer, they cannot screen efficiently the long-wavelength

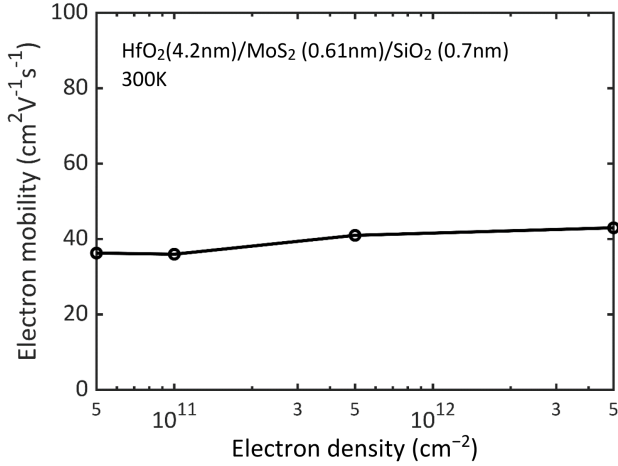


FIG. 11. Calculated 300 K electron mobility in the TMD channel of a $\text{HfO}_2/\text{MoS}_2/\text{SiO}_2$ structure as a function of the TMD free-carrier density. An electron sheet density of $5 \times 10^{12} \text{ cm}^{-2}$ has been assumed. The symbols represent calculated data, the lines are only a guide to the eye.

electron-phonon scattering processes. Additionally, degeneracy effects also affect the mobility: As the Fermi level increases, Pauli blocking prevents scattering to already occupied states, an effect that results in a higher mobility. However, this effect is partially compensated by the fact that, as the Fermi level increases, scattering to satellite valleys become effective, resulting in a reduction of the electron mobility. In the particular case of MoS_2 , these degeneracy effects cancel each other almost exactly and do not affect the mobility appreciably. This behavior can be expected also in other 2D TMDs. The weak dependence on the carrier sheet density shown in Fig. 11 has been observed experimentally by Pang *et al.* in FETs with thick ($>2 \text{ nm}$) TMD channels. [107].

v) Dependence on lattice temperature. The dependence of the electron mobility on temperature is shown in Fig. 12 for the the $\text{AlN}/\text{MoS}_2/\text{SiO}_2$, $\text{AlN}/\text{WS}_2/\text{SiO}_2$, and $\text{HfO}_2/\text{WS}_2/\text{SiO}_2$ double-gate system. A power law (shown by the solid black lines) yields the best correlation coefficient. However, it is difficult to assign to this fit a clear physical meaning, since several phonons with different frequencies contribute to the relaxation of the electron velocity. Comparing frames (a) and (b), the slightly larger frequency of the TMD ZO phonon seems to yield a slightly larger slope. The same observation can be made comparing frames (b) and (c): The softer optical phonons of HfO_2 result in a smaller slope (and a lower mobility).

We plot in Fig. 13 the temperature dependence of the electron mobility in the TMD monolayer in the $\text{AlN}/\text{WS}_2/\text{SiO}_2$ stack, showing separately the mobility limited only by the TMD ‘bulk’ phonons, μ_{rmBP} and the mobility limited only by scattering with the IPPs, μ_{IPP} . Note the weaker dependence on temperature of the former, since μ_{BP} is determined by the interaction with

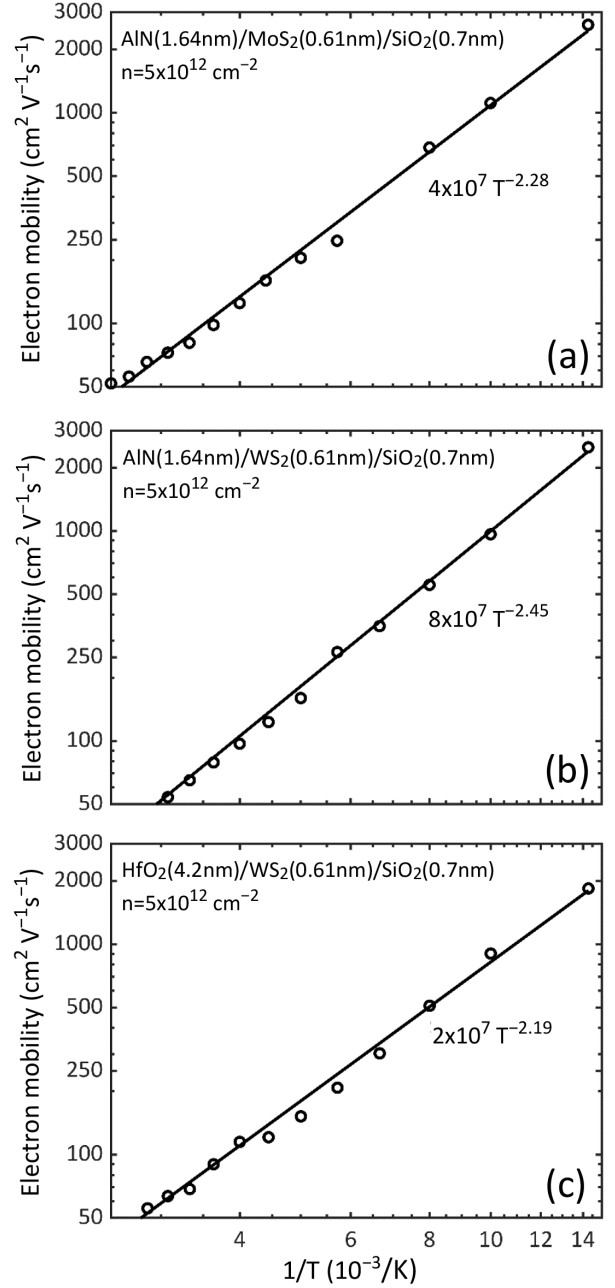


FIG. 12. Calculated electron mobility in the TMD channel of the (a) $\text{AlN}/\text{MoS}_2/\text{SiO}_2$, (b) $\text{AlN}/\text{WS}_2/\text{SiO}_2$, and (c) $\text{HfO}_2/\text{WS}_2/\text{SiO}_2$ structures as a function of lattice temperature. As in previous figures, the EOT of the insulators has been assumed to be 0.7 nm and the electron sheet density $5 \times 10^{12} \text{ cm}^{-2}$.

both low-energy ($\lesssim 20 \text{ meV}$) acoustic phonons and optical phonons with energy in the range of 40-to-50 meV. On the contrary, the IPP-limited mobility shows a stronger dependence on temperature, since it is controlled mainly by the interaction with the phonon component of hybrid modes originating from the higher-energy ($\sim 80 \text{ meV}$) AlN optical phonons. Scattering with the hybrid IPPs controls the mobility over the entire range of temper-

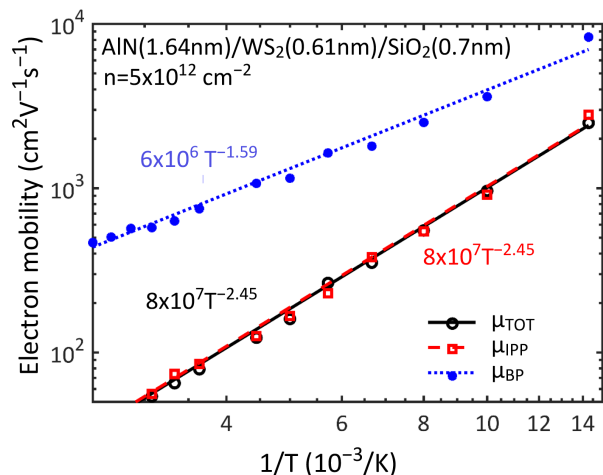


FIG. 13. Calculated bulk-phonon-limited, μ_{BP} , IPP-limited, μ_{IPP} , and total electron mobility, μ_{TOT} , in the TMD channel of an AlN/WS₂/SiO₂ stack, plotted *vs.* the lattice temperature. As in previous figures, the EOT of the insulators has been assumed to be 0.7 nm and the electron sheet density $5 \times 10^{12} \text{ cm}^{-2}$.

atures we have considered, although its relative importance decreases at low temperatures. It is interesting to note that the use of Matthiessen’s rule to estimate the total mobility as $\mu_{TOT} = [1/\mu_{BP} + 1/\mu_{IPP}]^{-1}$ results in a value that is underestimated by about 7% at 400 K, by about 17% at 70 K.

Power laws for the temperature dependence of the electron mobility in TMD monolayers have been observed experimentally at carrier densities in the range of the low 10^{11} s to the high 10^{12} s cm^{-2} , with data scattered significantly, not a surprising fact given the many process-dependent effects and deviations from ideality that unavoidably affect the measurements. To mention just a small set of experimental results reported in the literature, Wang and coworkers [108] found a power-law dependence, $\mu \sim T^{-\gamma}$, with an exponent γ of about 1.73 for WS₂ monolayers encapsulated by hBN. The mobility they report ranges from 800 $\text{cm}^2/(\text{V}\cdot\text{s})$ at 100 K to around 120 $\text{cm}^2/(\text{V}\cdot\text{s})$ at 300 K, values that, although not too dissimilar from the results shown in Figs. 12 and 13 in the presence of the high- κ AlN insulator, indicate the strong effect of additional scattering mechanisms, such as Coulomb scattering with charges defects. Indeed, for the same system, Xu *et al.* [109] have measured a steeper slope, with an exponent of about 1.9 – and of about 2.3 for similarly hBN-encapsulated MoS₂ monolayers – with a significantly higher mobility ranging from 3,000 $\text{cm}^2/(\text{V}\cdot\text{s})$ at 100 K to around 300 $\text{cm}^2/(\text{V}\cdot\text{s})$ at 200 K. An exponent of about 0.73, with mobilities in the range of 45 to 100 $\text{cm}^2/(\text{V}\cdot\text{s})$ between 250 and 100 K, has been observed by Ovchinnikov *et al.* [110] for back-gated MoS₂ monolayers on SiO₂. Also for back-gated MoS₂ supported by SiO₂, Smithe *et al.* [111] have measured an exponent of about 1.24 with a mobility decreasing from 200 $\text{cm}^2/(\text{V}\cdot\text{s})$ at 80 K to $\sim 35 \text{ cm}^2/(\text{V}\cdot\text{s})$

at 300 K, whereas an exponent of about 1.66, albeit with a very low mobility, has been reported in Ref. [112] for WS₂ monolayers, also on an SiO₂ substrate. Finally, Huo and coworkers [103] have measured an exponent of about 0.7 for the HfO₂/MoS₂/SiO₂ gate stack. The measured mobility varies from $\sim 80 \text{ cm}^2/(\text{V}\cdot\text{s})$ at 100 K to about 50 $\text{cm}^2/(\text{V}\cdot\text{s})$ at 300 K, low values probably due to the combined effect of IPP and additional scattering processes. With the exception of Ref. [108], that reports results from four-point probe measurements, and of Ref. [109], that reports both the Hall and the field-effect mobility – all experiments provide the field-effect mobility. In all cases, Coulomb scattering with defects, and even possible thermally-activated transport below 100 K [103] and variable-range hopping among traps in the low-temperature regime (20-to-250 K) [110], depresses the slope as well as the mobility, even showing saturation of the mobility below 100 K. Therefore it is not surprising to see a weaker dependence than what we have obtained for ideal monolayers in the absence of scattering with defects and hopping processes.

IV. CONCLUSIONS

We have investigated theoretically how, in addition to free-carrier screening, the dielectric environment (namely, the insulating substrate or bottom gate-insulator, the gate insulator, and the presence of metallic gates) affects the low-field charge-transport properties of several TMD monolayers supported (or back-gated) by SiO₂ and with hBN, SiO₂, AlN, Al₂O₃, HfO₂, and ZrO₂ as gate insulators, thus extending previous investigations to these realistic (and complicated) double-gate structures.

We have shown initially that, rescaling the electron-phonon scattering rates obtained from *ab initio* calculations for free-standing layers to account for the static screening effects of the surrounding dielectrics, high- κ dielectrics screen these interactions very efficiently. Although, in principle, this would result in an improved carrier mobility, unfortunately, the presence of these dielectrics also results in carriers scattering with the hybrid interface optical-phonon/plasmon excitations. Accounting for the full hybridization of these excitations also with the 2D TMD plasmons – an effect that we found is very important, but that is often ignored in the literature – we have shown that, as expected, this effect depresses the carrier mobility significantly below its value in free-standing monolayers, with the mobility increasing with increasing dielectric constant of the insulator(s). However, we have also found that ‘phonon resonances’ enhance the interface polarization charge and scattering potential, thus depressing the mobility even more severely. This occurs when two optical phonons of the dielectrics have similar frequencies and it results in an even stronger depression of the mobility.

Our results also show that the weak ionic polarizability

of hBN results in the highest electron and hole mobility, although the relatively low dielectric constant of this insulator negates the scaling benefits of high- κ insulators. They also show that tungsten-based TMDs exhibit a satisfactory carrier mobility. We have also found a weak dependence of the mobility on carrier density, that the dielectric screening effect of an ideal metal gate is noticeable in some cases (especially in TMDs that exhibit a high intrinsic mobility, such as WS₂), but not significantly strong. Unfortunately, in most cases the transport properties of TMDs remain disappointing, because of both the effects we have investigated here as well as, most likely, because of the intrinsic physical reasons discussed in Ref. [113].

ACKNOWLEDGMENTS

We are grateful to Jörg Appenzeller, Zhihong Chen, and Eric Pop for having shared preliminary experimen-

tal data and/or constructive discussions and to Edward Chen for support and encouragement. We also thank Mathieu Luisier for clarifications regarding Ref. [11] and Brian Ridley for many conversations that have clarified the confusion caused by the use of the term ‘remote phonon scattering’ to refer improperly to IPP scattering.

This work has been funded by the Semiconductor Research Corporation (SRC) nCORE/NEWLIMITS program and, in part, by the Taiwan Semiconductor Manufacturing Company Ltd. (TSMC).

Portions of this work were presented and published as an extended abstract at the 2022 International Conference on Simulation of Semiconductor Processes and Devices[114].

-
- [1] T. Sohler, D. Campi, N. Marzari, and M. Gibertini, *Phys. Rev. Mat.* **2**, 114010 (2018).
 - [2] S. Poncé, E. R. Margine, and F. Giustino, *Phys. Rev. B* **97**, 121201(R) (2018).
 - [3] Z. Jin, X. Li, J. T. Mullen, and K. W. Kim, *Phys. Rev. B* **90**, 045422 (2014).
 - [4] T. Gunst, T. Markussen, K. Stokbro, and M. Brandbyge, *Phys. Rev. B* **93**, 035414 (2013).
 - [5] A. Rawat, N. Jena, Dimple, and A. De Sarka, *J. Mat. Chem. A* **6**, 8693 (2018).
 - [6] K. Kaasbjerg, K. Thygesen, and K. Jacobsen, *Phys. Rev. B* **85**, 115317 (2012).
 - [7] O. D. Restrepo, K. E. Krymowski, J. Goldberger, and W. Windl, *New J. Phys.* **16**, 105009 (2014).
 - [8] X. Li, J. Mullen, Z. Jin, K. Borysenko, M. Nardelli, and K. Kim, *Phys. Rev. B* **87**, 115418 (2015).
 - [9] G. Gaddemane, S. Gopalan, M. L. Van de Put, and M. V. Fischetti, *J. Comput. Electron.* **20**, 49 (2021a).
 - [10] A. Szabó, R. Rhyner, and M. Luisier, *Phys. Rev. B* **95**, 035435 (2015).
 - [11] S. Fiore, C. Klinkert, F. Ducry, J. Backman, and M. Luisier, *Materials* **15**, 1062 (2022).
 - [12] S. Q. Wang and G. D. Mahan, *Phys. Rev. B* **6**, 4517 (1972).
 - [13] K. L. Kliever and R. Fuchs, *Phys. Rev.* **144**, 495 (1966).
 - [14] K. Hess and P. Vogl, *Solid State Commun.* **30**, 797 (1979).
 - [15] B. T. Moore and D. K. Ferry, *J. Appl. Phys.* **51**, 2603 (1980).
 - [16] F. Bechstedt and R. Enderlein, *Phys. Status Solidi (b)* **129**, 349 (1985).
 - [17] M. V. Fischetti, D. A. Neumayer, and E. A. Cartier, *J. Appl. Phys.* **90**, 4587 (2001).
 - [18] P. Toniutti, P. Palestri, D. Esseni, F. Driussi, M. De Michielis, and L. Selmi, *J. Appl. Phys.* **112**, 034502 (2012).
 - [19] S. Fratini and F. Guinea, *Phys. Rev. B* **77**, 195415 (2008).
 - [20] A. Konar, T. Fang, and D. Jena, *Phys. Rev. B* **82**, 115452 (2010).
 - [21] Z.-Y. Ong and M. V. Fischetti, *Phys. Rev. B* **88**, 045405 (2013a).
 - [22] E. H. Hwang and S. Das Sarma, *Phys. Rev. B* **87**, 115432 (2013).
 - [23] B. Scharf, V. Perebeinos, J. Fabian, and P. Avouris, *Phys. Rev. B* **87**, 035414 (2013).
 - [24] V. Perebeinos, S. V. Rotkin, A. G. Petrov, and P. Avouris, *Nano Lett.* **9**, 312 (2009).
 - [25] K. Xiu, in *2011 International Conference on Simulation of Semiconductor Processes and Devices (IEEE, 2011)*, pp. 35–38.
 - [26] R. Egdell, W. Flavell, Z. Gray-Grychowski, R. Stradling, B. Joyce, and J. Neave, *J. Electron Spectrosc. Relat. Phenom.* **45**, 177 (1987).
 - [27] P. Y. Yu and M. Cardona, in *Fundamentals of Semiconductors* (Springer, 1996), pp. 17–105.
 - [28] D. Hagenmüller, J. Schachenmayer, C. Genet, T. W. Ebbesen, and G. Pupillo, *ACS Photonics* **6**, 1073 (2019).
 - [29] S. Ribeiro, A. Vasanelli, Y. Todorov, and C. Sirtori, in *Photonics* (Multidisciplinary Digital Publishing Institute, 2020), vol. 7, p. 19.
 - [30] J.-j. Shi, *Phys. Rev. B* **68**, 165335 (2003).
 - [31] R. Singh, M. Dutta, M. A. Stroschio, A. G. Birdwell, and P. M. Amirtharaj, *J. Appl. Phys.* **125**, 205704 (2019).
 - [32] L. Zeng, Z. Xin, S. Chen, G. Du, J. Kang, and X. Liu, *Appl. Phys. Lett.* **103**, 113505 (2013).
 - [33] N. Ma and D. Jena, *Phys. Rev. X* **4**, 011043 (2014).
 - [34] M. Hosseini, M. Elahi, M. Pourfath, and D. Esseni, *IEEE Trans. Electron Dev.* **62**, 3192 (2015).
 - [35] P. Chang, X. Liu, F. Liu, and G. Du, *Micromachines* **9**, 674 (2018).
 - [36] A. Hauber and S. Fahy, *Phys. Rev. B* **95**, 045210 (2017).
 - [37] Q. Zhang, Z. Zhen, Y. Yang, G. Gan, D. Jariwala, and X. Cui, *Opt. Express* **27**, 18585 (2019).
 - [38] A. Dyson and B. K. Ridley, arXiv:2004.06454 (2020).
 - [39] S. Saito, K. Tirii, M. Hiratani, and T. Onai, *Appl. Phys.*

- Lett. **81**, 2391 (2002).
- [40] F. Gámiz, J. B. Roldán, J. E. Carceller, and P. Cartujo, Appl. Phys. Lett. **82**, 3251 (2003).
- [41] S. Barraud, L. Thevenod, M. Cassé, O. Bonno, and M. Mouis, Microelectron. Eng. **84**, 2404 (2007).
- [42] D. Esseni and A. Abramo, IEEE Trans. Electron Dev. **50**, 1665 (2015).
- [43] H. Ota, A. Hirano, Y. Watanabe, N. Yasuda, K. Iwamoto, K. Akiyama, K. Okada, S. Migita, T. Nabatame, and A. Toriumi, in *IEDM Technical Digest. IEEE International Electron Devices Meeting, 2004.* (IEEE, 2007), pp. 65–68.
- [44] R. Chau, S. Datta, M. Doczy, B. Doyle, J. Kavalieros, and M. Metz, IEEE Trans. Electron Dev. **25**, 408 (2004).
- [45] A. M. Sonnet, R. V. Galatage, P. K. Hurley, E. Pelucchi, K. Thomas, A. Gocalinska, J. Huang, N. Goel, G. Bersuker, W. P. Kirk, et al., Microelectron. Eng. **88**, 1083 (2011).
- [46] Z. Yu, Z.-Y. Ong, Y. Pan, Y. Ciu, Y. Xin, Run agnd Shi, B. Wanf, Y. Wu, T. Chen, Y.-W. Zhang, G. Zhang, et al., Adv. Mater. **28**, 547 (2016).
- [47] H. Tanimoto, M. Kondo, T. Enda, N. Aoki, R. Iijima, T. Watanabe, M. Takayanagi, and H. Ishiuchi, in *2006 International Conference on Simulation of Semiconductor Processes and Devices* (2006), pp. 47–50.
- [48] K. Maitra, M. F. Martin, V. Narayanan, V. Misra, and E. A. Cartier, J. Appl. Phys. **102**, 114507 (2007).
- [49] Y. X. Ma, H. Su, W. M. Tang, and P. To Lai, IEEE Electron Device Lett. **40**, 893 (2019).
- [50] H. Su, W. M. Tang, and P. To Lai, J. Appl. Phys. **130**, 015302 (2021).
- [51] B. Laikhtman and P. Solomon, J. Appl. Phys. **103**, 014501 (2008).
- [52] R. Kotlyar, M. Giles, P. Matagne, B. Obradovic, L. Shifren, M. Stettler, and E. Wang, in *IEDM Technical Digest. IEEE International Electron Devices Meeting, 2004.* (IEEE, 2004), pp. 391–394.
- [53] R. Shah and M. M. De Souza, IEEE Trans. Electron Dev. **54**, 2991 (2007).
- [54] S. A. B. Suleiman, H.-J. Oh, and S. Lee, IEEE Trans. Electron Dev. **59**, 1377 (2012).
- [55] Although semiconducting hexagonal WTe₂ monolayers are unstable at room temperature (as shown, for example, by Lee *et al.*, Sci. Rep. **5**, 10013 (2015)), Huang and coworkers, Phys. Chem. Chem. Phys. **18**, 4086 (2016), have used DFT to show that the energy-barrier that separates the lowest-energy phase – the metallic distorted 1T' (Td) phase – from the 2H phase, is about 0.77 eV. This suggests that the hexagonal phase may be metastable. Indeed, recently Li *et al.*, Inorg. Chem. **59**, 11935 (2020), have employed a lithium-intercalation process to synthesize semiconducting 2H WTe₂ nanosheets that are stable at 300 K. For this reason, and for the interest that WTe₂ has attracted, we consider it here, although some may view 2H WTe₂ monolayers as 'hypothetical' since, so far, there has been no study providing experimental evidence of its semiconducting charge-transport properties or, even more important, of its use as channel material in FETs.
- [56] A. Laturia, M. L. Van de Put, and W. G. Vandenberghe, npj 2D Mater. Appl. **2**, 1 (2018).
- [57] T. Tian, D. Scullion, D. Hughes, L. H. Li, C.-J. Shih, J. Coleman, M. Chhowalla, and E. J. Santos, Nano Lett. **20**, 841 (2019).
- [58] F. Stern, Phys. Rev. Lett. **18**, 546 (1967).
- [59] J. Z. Zhang, AIP Adv. **10**, 045316 (2020).
- [60] P. F. Maldague, Surf. Sci. **73**, 296 (1978).
- [61] G. Vignale, Phys. Rev. B **38**, 811 (1987).
- [62] P. Giannozzi, S. Baroni, N. Bonini, M. Calandra, R. Car, C. Cavazzoni, D. Ceresoli, G. L. Chiarotti, M. Cococcioni, I. Dabo, et al., J. Phys.: Cond. Matt. **21**, 395502 (2009).
- [63] J. P. Perdew, K. Burke, and M. Ernzerhof, Phys. Rev. Lett. **77**, 3865 (1996).
- [64] D. Hamann, Phys. Rev. B **88**, 085117 (2013).
- [65] G. Gaddemane, W. G. Vandenberghe, M. L. Van de Put, S. Chen, S. Tiwari, E. Chen, and M. V. Fischetti, Phys. Rev. B **98**, 115416 (2018).
- [66] G. Gaddemane, M. L. Van de Put, W. G. Vandenberghe, E. Chen, and M. V. Fischetti, J. Comput. Electron. **20**, 60 (2021b).
- [67] F. Giustino, M. L. Cohen, and S. G. Louie, Phys. Rev. B **76**, 165108 (2007).
- [68] S. Baroni, S. De Gironcoli, A. Dal Corso, and P. Giannozzi, Rev. Mod. Phys. **73**, 515 (2001).
- [69] F. Giustino, Rev. Mod. Phys. **89**, 015003 (2019a).
- [70] F. Giustino, Rev. Mod. Phys. **91**, 019901 (2019b).
- [71] D. Alfé, Comput. Phys. Commun. **180**, 2622 (2009).
- [72] Z.-Y. Ong and M. V. Fischetti, Phys. Rev. B **86**, 165422 (2012).
- [73] E. A. Stern and R. A. Ferrell, Phys. Rev. **120**, 130 (1960).
- [74] B. Ridley, *Quantum processes in semiconductors* (Oxford Science Publications, 1999).
- [75] B. B. Varga, Phys. Rev. **137**, A1896 (1965).
- [76] M. E. Kim, A. Das, and S. D. Senturia, Phys. Rev. B **18**, 6890 (1978).
- [77] P. G. Klemens, Phys. Rev. **148**, 845 (1966).
- [78] J. M. Ziman, *Electrons and Phonons: The Theory of Transport Phenomena in Solids* (Oxford university press, 2001).
- [79] S. A. Egorov and J. L. L. Skinner, J. Chem Phys. **103**, 1555 (1995).
- [80] A. Berke, A. P. Mayer, and R. K. Wehner, J. Phys.C: Solid State Phys. **21**, 2305 (1988).
- [81] T. Feng and X. Ruan, Phys. Rev. B **93**, 045202 (2016).
- [82] S.-D. Guo, Phys. Chem. Chem. Phys. **20**, 7236 (2018).
- [83] L. Landau, The Collected Papers of LD Landau pp. 445–460 (1965).
- [84] D. Pines and J. R. Schrieffer, Phys. Rev. **124**, 1387 (1961).
- [85] D. Pines and J. R. Schrieffer, Phys. Rev. **125**, 804 (1962).
- [86] D. Bohm and D. Pines, Phys. Rev. **92**, 609 (1953).
- [87] R. Tsu, Phys. Rev. **164**, 380 (1967).
- [88] J. J. Quinn and R. A. Ferrell, Phys. Rev. **112**, 812 (1958).
- [89] J. J. Quinn, Phys. Rev. **126**, 1453 (1962).
- [90] D. R. Penn, Phys. Rev. B **35**, 482 (1987).
- [91] D. R. Penn, VLSI Design **6**, 69 (1998).
- [92] M. V. Fischetti and W. G. Vandenberghe, Phys. Rev. B **932**, 155413 (2016a).
- [93] M. V. Fischetti and W. G. Vandenberghe, *Advanced Physics of Electron Transport in Semiconductors and Nanostructures* (Springer, 2016b).
- [94] E. Mariani and F. Von Oppen, Phys. Rev. Lett. **100**, 076801 (2008).

- [95] F. Von Oppen, F. Guinea, and E. Mariani, *Phys. Rev. B* **80**, 075420 (2009).
- [96] K. I. Bolotin, K. J. Sikes, J. Hone, H. Stormer, and P. Kim, *Phys. Rev. Lett* **101**, 096802 (2008).
- [97] E. Castro, H. Ochoa, M. Katsnelson, R. Gorbachev, D. Elias, K. Novoselov, A. Geim, and F. Guinea, *Phys. Rev. Lett* **105**, 266601 (2010).
- [98] I. Gornyi, V. Y. Kachorovskii, and A. Mirlin, *Phys. Rev. B* **86**, 165413 (2012).
- [99] A. Rudenko, A. Lugovskoi, A. Mauri, G. Yu, S. Yuan, and M. Katsnelson, *Phys. Rev. B* **100**, 075417 (2019).
- [100] C. Jacoboni and L. Reggiani, *Rev. Mod. Phys.* **55**, 645 (1983).
- [101] B. Radisavljevic, A. Radenovic, J. Brivio, V. Giacometti, and A. Kis, *Nat. Nanotech.* **6**, 147 (2011).
- [102] B. Radisavljevic and A. Kis, *Nat. Mater.* **12**, 815 (2013).
- [103] N. Huo, Y. Yang, Y.-N. Wu, X.-G. Zhang, S. T. Pantelides, and G. Konstantatos, *Nanoscale* **10**, 15071 (2018).
- [104] Z.-Y. Ong and M. V. Fischetti, *Phys. Rev. B* **88**, 165316 (2013b).
- [105] R. A. Horn and C. R. Johnson, *Matrix Analysis* (Cambridge University Press, 1985).
- [106] M. L. Van de Put, G. Gaddemane, S. Gopalan, and M. V. Fischetti, in *2020 International Conference on Simulation of Semiconductor Processes and Devices (SISPAD)* (IEEE, 2020), pp. 281–284.
- [107] C.-S. Pang, R. Zhou, X. Liu, P. Wu, T. Y. T. Hung, S. Guo, M. E. Zaghoul, S. Krylyuk, A. V. Davydov, J. Appenzeller, et al., *Small* **17**, 2100940 (2021).
- [108] Y. Wang, T. Sohler, K. Watanabe, T. Taniguchi, M. J. Verstraete, and E. Tutuc, *Appl. Phys. Lett.* **118**, 102105 (2021).
- [109] S. Xu, Z. Wu, H. Lu, Y. Han, G. Long, X. Chen, T. Han, W. Ye, Y. Wu, J. Lin, et al., *2D Mater.* **3**, 021007 (2016).
- [110] D. Ovchinnikov, A. Allain, Y. S. Huang, D. Dumcenco, and A. Kis, *ACS Nano* **8**, 8174 (2014).
- [111] K. K. H. Smithe, C. D. English, S. V. Suryavanshi, and E. Pop, *Nano Lett.* **18**, 4516 (2018).
- [112] A. Alharbi and D. Shahrjerdia, *Appl. Phys. Lett.* **109**, 193502 (2016).
- [113] L. Cheng, C. Zhang, and Y. Lui, *Phys. Rev. Lett.* **125**, 177701 (2020).
- [114] S. Gopalan, M. L. Van de Put, G. Gaddemane, and M. V. Fischetti, *Solid State Electron.* **TBD**, TBD (2022), Special issue on the Proceedings of the 2022 *International Conference on Simulation of Semiconductor Processes and Devices* (SISPAD 2022).